Université de Montréal

Position Measurement Of The SuperCDMS HVeV Detector And Implementation Of An Importance Sampling Algorithm In The SuperCDMS Simulation Software

par

David Santiago Pedreros

Département de physique
Faculté des arts et des sciences

Mémoire présenté en vue de l'obtention du grade de
Maître ès sciences (M.Sc.)
en Physique

April 29, 2023

Université de Montréal

Faculté des arts et des sciences

Ce mémoire intitulé

Position Measurement Of The SuperCDMS HVeV Detector And Implementation Of An Importance Sampling Algorithm In The SuperCDMS Simulation Software

présenté par

David Santiago Pedreros

a été évalué par un jury composé des personnes suivantes :

Jean-François Carrier
(président-rapporteur)

Alan Robinson
(directeur de recherche)

Louis-André Hamel
(membre du jury)

Résumé

La matière sombre est considérée comme l'un des plus grands mystères dans la cosmologie moderne. En effet, on peut dire que l'on connaît plus sur ce que la matière sombre n'est pas que sur sa vraie nature. La collaboration SuperCDMS travaille sans répit pour réussir à faire la première détection directe de la matière sombre. À cet effet, la collaboration a eu recours à plusieurs expériences et simulations à diverses échelles, pouvant aller de l'usage d'un seul détecteur semi-conducteur, jusqu'à la création d'expériences à grande échelle qui cherchent à faire cette première détection directe de la matière sombre. Dans ce texte, on verra différentes méthodes pour nous aider à mieux comprendre les erreurs systématiques liées à la position du détecteur utilisé dans le cadre des expériences IMPACT@TUNL et IMPACT@MTL, soit l'usage des simulations et de la radiologie industrielle respectivement. On verra aussi comment l'implémentation de la méthode de réduction de variance connue comme échantillonnage préférentiel, peut aider à améliorer l'exécution des simulations de l'expérience à grande échelle planifiée pour le laboratoire canadien SNOLAB. En outre, on verra comment l'échantillonnage préférentiel s'avère utile non seulement pour mieux profiter des ressources disponibles pour la collaboration, mais aussi pour avoir une meilleure compréhension des source de bruits de fond qui seront présentes à SNOLAB, tels que les signaux générés par la désintégration radioactive de divers isotopes.

Mots-clé: matière sombre, detection directe, SuperCDMS, simulation, radiologie industrielle, réduction de variance, échantillonnage préférentiel

Abstract

Dark matter is one of the biggest mysteries of modern-day cosmology. Simply put, we know much more about what it is not, rather than what it actually is. The SuperCDMS collaboration works relentlessly toward making the first direct detection of this type of matter. To this effect, multiple experiments and simulations have been performed, ranging from small-scale testing of the detectors to large-scale, long-term experiments, looking for the actual detection of dark matter. In this work, I will analyze different methods to help understand the systematic errors linked to detector position in regard to the small-scale experiments IMPACT@TUNL and IMPACT@MTL, through simulation and industrial radiography respectively. We will also see how the implementation of the variance reduction method known as importance sampling can be used to improve the simulation performance of the large-scale experiment in the Canadian laboratory SNOLAB. Additionally, we will see how this method can provide not only better management of the computing resources available to the collaboration, but also how it can be used to better the understanding of the background noises, such as the signals generated by radioactive decay of different isotopes, that will be present at SNOLAB.

Keywords: dark matter, direct detection, SuperCDMS, simulation, industrial radiography, variance reduction, importance sampling

Contents

Résumé 5

Abstract 7

List of Tables 11

List of Figures 13

List of Acronyms and Abreviations 15

Acknowledgements 17

Introduction 19

Chapter 1. Position Measurement of HVeV Detector Inside the ADR Used by the IMPACT Experiment 23

1.1. The IMPACT Experiment 23
1.1.1. Ionization Yield: State of the Field 25

1.2. Nuclear Recoil Theory 27

1.3. The Position Of the HVeV Detector 30
1.3.1. Simulations: Independent Motion of the HVeV Detector Within the ADR . 30
1.3.2. Industrial Radiography 32
1.3.2.1. Experimental Setup 32
1.3.2.2. Film Processing 33
1.3.2.3. Position reconstruction 35

Chapter 2. Implementation of an Importance Sampling Algorithm in the Context of the Simulations Software SuperSim 39

2.1. Variance Reduction in Monte Carlo Simulations 39
2.1.1. Importance Biasing in Geant4 41
2.1.1.1. The Algorithm 41

2.2. Importance Sampling Implementation in SuperSim 42
2.2.1. The Geometry 44
2.2.2. The Physics List 47
2.2.3. Validation Study of the Implementation 48
2.2.3.1. The Initial Conditions 48
2.2.3.2. Results and discussion 49

References 53

Appendix A. Tower Assembly Work 55

List of Tables

1.1 Calculated transmissions through the materials 33

2.1 Table summarizing the used computing resources 52

List of Figures

0.1 Event histogram as a function of the phonon energy and the amplification energy in the silicon HVeV detector, taken from [**18**] 20

1.1 ADR mounted at the Montreal beamline 24

1.2 Results of the IMPACT@TUNL experiment. Publication in preparation 26

1.3 kinematics diagram for nuclear recoil. 27

1.4 Ionization yield for Simulated and CAD positions 31

1.5 Scanned Image of films 1 and 2 34

1.6 Scanned Image of film 3 34

1.7 Enhanced image of film 1 35

1.8 Reconstruction diagram for a 15° rotation. 36

1.9 Reconstruction diagram for a 19° rotation. 36

1.10 Close-up on the reconstruction diagram for a 15° rotation. 36

1.11 Close-up on the reconstruction diagram for a 19° rotation. 36

2.1 Splitting routine applied at the boundaries between 2 cells. 42

2.2 Russian Roulette routine applied at the boundaries between 2 cells. 42

2.3 Raw background spectra of single-scatter interactions in a Si (left) and Ge (right) detector obtained from the MCMC simulation. The spectra are broken down into components and shown as functions of recoil energy (Electron Recoil or Nuclear Recoil depending on the interaction). ^{3}H (pink) and ^{32}Si (purple) are the largest individual contributors to the backgrounds in the Ge and Si detectors, respectively. The remaining components are Compton scatters from gamma rays (red), surface betas (green), surface ^{206}Pb recoils (orange), neutrons (blue),‘ and coherent elastic neutrino-nucleus scattering (cyan). Note that the neutron spectrum (blue) has some spurious structure from the limited simulation statistics in the cavern component of the neutron background. Figure taken from [**1**] 44

2.4 Top view from the SNOLAB geometry and an enlarged view of the layers of interest 45
2.5 Histogram of the particle types recorded at the inner poly in the unbiased simulation. 49
2.6 Histogram of the particle types recorded at the inner poly in the biased simulation. 49
2.7 Gamma energy spectrum for the unbiased simulation. 50
2.8 Gamma energy spectrum for the biased simulation. 50
2.9 Lead lines in the unbiased gamma spectrum. 50
2.10 Lead lines in the biased gamma spectrum. 50
2.11 Electron energy spectrum for the unbiased simulation. 51
2.12 Electron energy spectrum for the biased simulation. 51

List of Acronyms and Abreviations

ADR	**A**diabatic **D**emagnetization **R**efrigerator
HVeV	**H**igh **V**oltage **e**lectron**V**olt resolution
IMPACT	**I**onisation **M**easurement with **P**honons **A**t **C**ryogenic **T**emperatures
MCMC	**M**arkov **C**hain **M**onte **C**arlo
SNOLAB	**S**udbury **N**eutrino **O**bservatory Laboratory
SuperCDMS	Super **C**ryogenic **D**ark **M**atter **S**earch
WIMP	**W**eakly **I**nteractive **M**assive **P**article

Acknowledgements

First, I would like to thank my parents, Rafael Pedreros and Yadira Fonseca, for their unyielding support and immense love. I would also like to thank my brother, Leonardo Pedreros, for all the good laughs we have shared and the memories created during our trips together.

I wish to thank my research supervisor, Dr. Alan Robinson, for granting me the opportunity to join his research team, for relighting my passion for physics, and for all his guidance and advice through my degree. I thank my colleagues at the bunker: Émile, Jeremy, Valerie, Noah and Mathieu, and my colleagues at SuperCDMS, particularly Ziqing, Birgit and Mike.

I am grateful as well for my close friends Haechan Mark Bong, Zongpu Zed Zheng, Wei Peng Cai, and Gabriel Rezende for their constant encouragement during my degree, their patience when I made them go through lengthy explanations of my work that would also help me clear and simplify my train of thought, and their support, especially during our "productivity sprints" that were so useful to get our own work done during the pandemic. Finally, a special thanks go to my little dog, Lanna, who would burst into my room at random times to demand to go on a walk, unknowingly helping me to have a much-needed break in moments of high stress.

Introduction

To this day, dark matter proves to be a great challenge for physicists around the world, as it only way we know of its existence is because of its gravitational effects, but a direct detection is yet to be made. The first hints towards its existence came from Fritz Zwicky's work in the 1930s; he coined the term "Dark matter" for the missing mass in his research on the Coma galaxy cluster. During the next 90 years, the evidence of the presence of dark matter accumulated with multiple examples like the rotational speeds of galaxies and the missing mass in certain gravitational lenses. However, after many decades of hunting for it in the night sky, with particle accelerators, and in underground experiments, the scientific community still does not have a clear understanding of the nature of this type of matter, seeing that no direct detection has been made.

With the objective of making this first direct detection, the SuperCDMS (Super Cryogenic Dark Matter Search) collaboration gathers the efforts of 29 universities across 3 continents and focuses their research on a kind of particle considered to be one of the best candidates for a dark matter particle: the WIMP (Weakly Interactive Massive Particle). The next iteration of SuperCDMS plans to place multiple germanium and silicon-based cryogenic detectors in the underground installations of the Canadian laboratory SNOLAB (Sudbury Neutrino Observatory Laboratory). One type of detector that will be used is the HVeV (High Voltage electronVolt resolution) model. The HVeV detector is one of the great successes of the SuperCDMS, as it is capable of measuring the ionization of single e-h (electron-hole) pairs produced by the elastic recoil of a neutron on the crystal lattice of the silicon or germanium heart of the detector. As figure 0.1 shows, the events are clearly quantized in peaks at given energies, measured in total collected energy in eV (eVt) from the phonons, or in electron equivalent energy scale (eVee). This remarkably high sensitivity is achieved by exploiting different quantum phenomena. Simply put, a nuclear recoil on the HVeV crystal produces an initial ionization and phonon such that their summed energy is equal to the energy deposited by the recoil. The high voltage across the crystal then accelerates the ionized electrons and holes, which produce more phonons on their path, effectively amplifying the initial ionization signal. This amplified energy is then absorbed through the chain of quantum devices that measure heat. This way, the HVeV detector allows relating the nuclear recoil energy, which

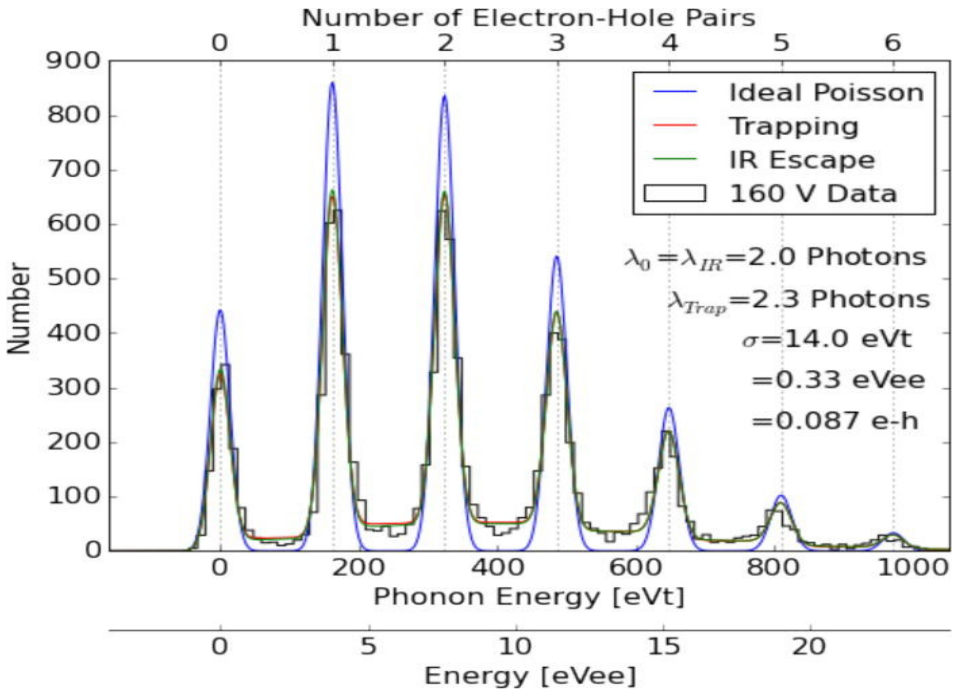

Figure 0.1. Event histogram as a function of the phonon energy and the amplification energy in the silicon HVeV detector, taken from [**18**]

is in the order of a few electronVolts, to a number of e-h pairs in the detector, through the measured phonon energy.

One of the challenges that come together with the extremely high sensitivity of the HVeV detector is the necessity to understand all the sources of background signals as much as possible. That is why much work has also been put into studying and reducing all sources of background noise, be it through shielding, developing protocols to minimize contamination and cosmic activation, or simulation of different scenarios. To reach these goals, SuperCDMS has also executed some other small-scale experiments to test and characterize all the components that make up the SNOLAB version. Among these small-scale studies, we find the IMPACT (Ionisation Measurement with Phonons At Cryogenic Temperatures) project. This sub-experiment of SuperCDMS used an ADR (Adiabatic Demagnetization Refrigerator) to cool down one of the detector models used by the collaboration: the HVeV detector. In the most recent trial run of IMPACT at the Tandem facilities from the Université de Montreal, a silicon-based HVeV detector was bombarded with 4.8 keV neutrons generated by accelerating protons on a Vanadium-51 target. In fact, my work in the context of the SuperCDMS collaboration is focused on two fronts: the HVeV detector used in the IMPACT experiment and the lead that will be used on the bigger iteration of SuperCDMS at SNOLAB.

In this work, chapter one will present a description of nuclear recoil theory and its importance for the IMPACT setup and experiment. It will discuss my efforts in the understanding

of the IMPACT geometry, namely the execution of industrial radiography to infer the position of the HVeV detector inside the ADR after it reached operating temperatures, as well as the improvement of our simulation software to account for a displacement of the detector during cool down, or a possible misalignment of the beam during operation.

On the other hand, Chapter two will present my work on the event biasing technique known as importance sampling on our simulation software. This algorithm is used to try to produce the most realistic simulation of the propagation of particles inside a solid material possible; specifically, it was applied to gamma particles propagating through the lead shield of the SNOlAB configuration. My work aimed at integrating, testing, and validating the importance biasing technique on the lead shield with respect to the standard performance of the simulation.

Chapter 1

Position Measurement of HVeV Detector Inside the ADR Used by the IMPACT Experiment

1.1. The IMPACT Experiment

The IMPACT experiment aims to measure the ionization yield for nuclear recoils in silicon. Such measurements have been performed multiple times for other elements, such as Argon[**14**], Xenon[**15**], and Sodium through Sodium activated cesium iodide[**5**], to name a few. The technique depends on the fact that the amount of ionization for a given recoil energy depends on the type of recoil. An interaction with the electrons, which corresponds to the sources used for a first calibration, will produce more electron-hole pairs than a nuclear recoil, which is the kind of signal that dark matter would produce. Therefore, running an experiment with a beam of uncharged particles that would scatter off the nuclei of the detector crystal will help us to calibrate the HVeV detector for a nuclear recoil signal. In addition, a set of backing detectors are used to measure the recoil angle of the neutrons. Generally, these backing detectors are composed of 2 stages, the first one of which is made of a scintillating material that produces some photons which will then be picked up at the next stage with a Photomultiplier Tube (PMT). Knowing this angle will allow us to know the energy deposited in the silicon crystal as explained in section 1.2. This way, it is possible to relate the average energy necessary to generate an electron-hole pair (ϵ), the energy deposited (E_{recoil}), the amount of electron-hole pairs (n_{eh}) generated and the ionization yield (Y) through the following equation:

$$n_{eh} = Y \cdot \frac{E_{recoil}}{\epsilon} \tag{1.1.1}$$

With the first results of the experiment coming from the run at the TUNL laboratory (IMPACT@TUNL), the objective of running IMPACT at the Montreal facilities (IMPACT@MTL) is to use low-energy neutrons as their signal would be more in line with the one produced by a dark matter particle scattering of the germanium model of the HVeV detector. However, pushing for low-energy neutrons comes with a few challenges. Even if Montreal's Tandem accelerator can reach a higher current, it is not capable of producing a bunched beam, which rules out the usage of a time of flight measurement to discriminate between neutrons and photons. Another challenge is the fact that given the low energy of the neutrons, it is very hard to detect the scattered neutrons with the backing detectors. Indeed, the quenching factor of most of the commercially available liquid scintillators that are used in these detectors does not allow the neutrons to deposit energy higher than the PMT's threshold. To counter this, the group plans to use boronated liquid scintillators and PMTs for the backing detectors. A slow neutron interacting with the boron atoms produces a high-energy gamma particle, which can be easily detected by the liquid scintillators and be well above the threshold for the PMTs. The last challenge to face is the fact that the low neutron energy is far from the Silicon resonant energy for elastic scattering, which means that the interaction rate will be much lower than the IMPACT@TUNL iteration.

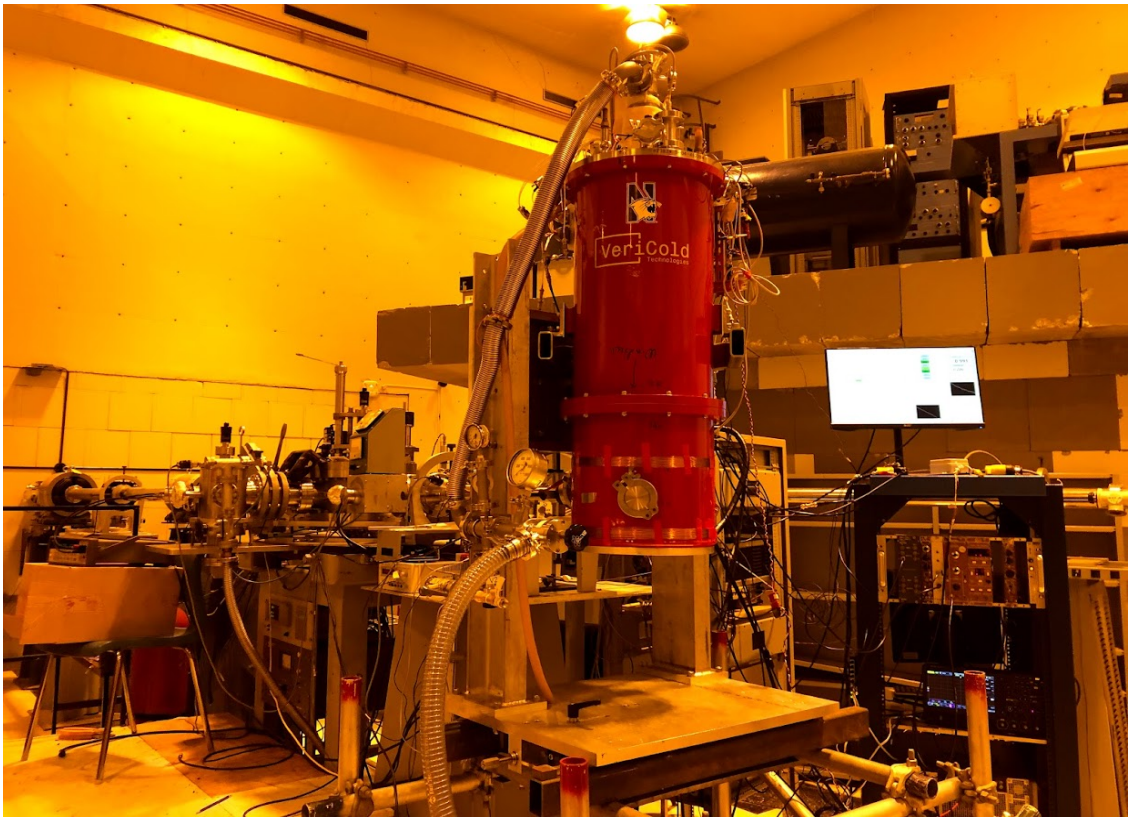

Figure 1.1. ADR mounted at the Montreal beamline

A first attempt was performed during the summer of 2021 (see figure 1.1). Apart from testing the procedures and equipment, our objective was to check the feasibility of the experiment; that is, if we would be able to produce low-energy neutrons and see a signal in the HVeV detector coming from their scattering. To generate the neutrons, the Tandem accelerator produced 1.566 MeV protons that bombarded a natural Vanadium target. Considering that the target is composed at $99,75\%$[**6**] of the isotope (^{51}V), the bombardment produced a monoenergetic beam of 4.8 keV neutrons through the reaction ^{51}V(p,n)^{51}Cr [**11**]. Next, the ADR was aligned to be at either 0° or 15°, and the data was recorded. During this run, the data analysis was performed by Ph.D. candidate Émile Michaud, while I took care of the work related to the industrial radiography described in section 1.3.2. The results of the first IMAPCT@MTL run proved to be successful, as the analysis showed a neutron rate count at the HVeV detector of 0.007 Hz, or about 25 neutrons scattered per hour.

1.1.1. Ionization Yield: State of the Field

The initial theory predicting the ionization yield in silicon was devised by J. Lindhard, V. Nielsen, M. Scharff, and P. Thomsen [**16**] in the 1960s, and is most commonly known as the Lindhard model. This model was then tested by Sattler[**19**] at Los Alamos Scientific Laboratory with their 8 MeV Van de Graaf accelerator. Sattler used as well a 180 keV neutron generator at the Sandia Corporation. He also set up the general method to perform this measurement, as he used a solid-state silicon detector to measure the energy deposition of the neutrons, and a plastic scintillator to measure the scattering angle. His results found a good agreement with the Lindhard model.

Later in 1990, G. Gerbier et al. [**10**] executed the same measurement with the 4 MeV Van de Graaff accelerator of the Centre d'Etudes Nucléaires de Bruyères-le-Chatel. Their setup produced 200 keV neutrons and they also found a good agreement with the Lindhard model. In the same year, another ionization yield measurement was performed at the Ohio University Tandem Van de Graaff laboratory by Zecher et al [**21**]. His group used 1.4 MeV neutrons on a 5.7 g silicon detector and his results not only agreed with the Lindhard model but were also consistent with Sattler's results. The final iteration in the 20^{th} century was done by Brian Dougherty in 1992 [**8**]. His experiment used the 3 MeV Van de Graaff accelerator at Lockheed's Applied Physics Research Laboratory, where he used 56, 189, 566, and 815 keV neutrons. His results were the first to show a disagreement with the ones produced by Gerbier et al and those by Zecher et al; with Dougherty's results, therefore, diverging from the predictions in the Lindhard et al model.

After the turn of the century, two more measurements were made; the first one was done by Chavarria et al [**4, 20**] in 2015, and the second was performed by F. Izraelevitch et al [**13**] in 2017. In the first experiment, Chavarria's group used a photoneutron source to obtain a

nearly monochromatic neutron beam with an energy of 24 keV. These were scattered on a low-threshold 2.2-g silicon charge-coupled device (CCD) created by the DAMIC experiment. Here again, the results did not match the predictions of the Lindhard model. Finally, The Antonella experiment used the FN Tandem Van de Graaff accelerator of the Institute for Structure and Nuclear Astrophysics (University of Notre Dame, Indiana) and was led by the Izraelevitch et al group. They used a neutron energy range going from 0 to 600 keV and their results are compatible with those from Chavarria et al, showing a discrepancy with the Lindhard model.

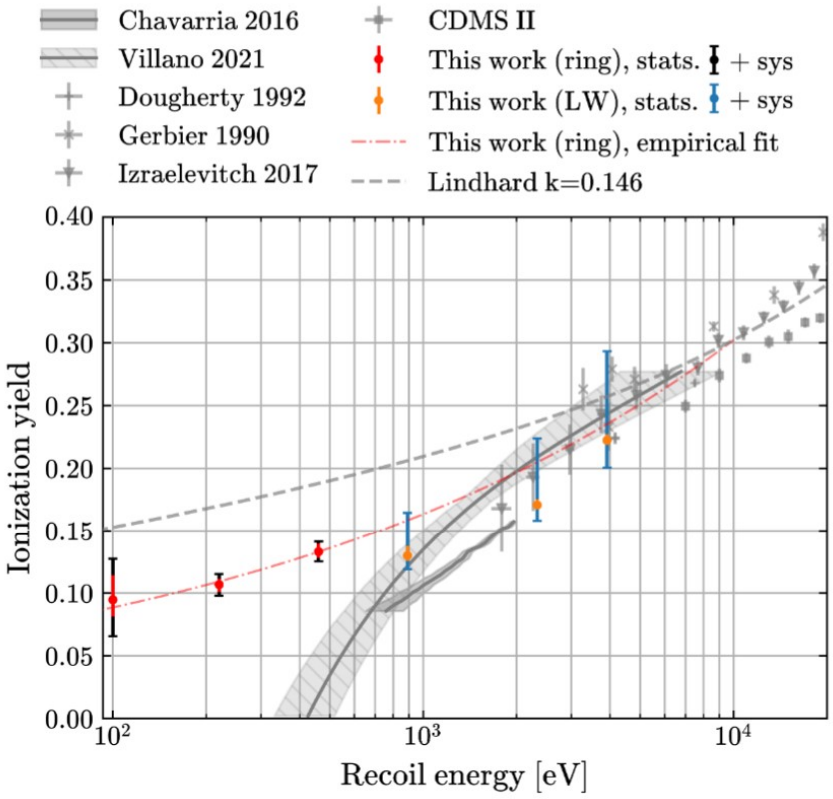

Figure 1.2. Results of the IMPACT@TUNL experiment. Publication in preparation

Most recently, the SuperCDMS collaboration completed an ionization yield measurement with the IMPACT@TUNL experiment. This iteration of IMPACT accelerated protons onto a lithium fluoride target, creating neutrons at around 11 keV and 56 keV through the reaction ^{7}Li(p,n)^{7}Be. The neutrons would scatter on the cryogenic silicon detector HVeV, which amplifies the signal through the Neganov-Trofimov-Luke effect. The neutrons are captured later on with a set of liquid scintillators and PMTs placed at specific scattering angles. Although the results have not been officially published yet, it is no surprise that the model for the ionization yield deviates from the Lindhard model, most notably at low recoil energies. Figure 1.2 summarizes the results from previous studies, the Lindhard model, and the

IMPACT@TUNL results, and it is clear that the ionization yield drops below the Lindhard model at lower recoil energies.

1.2. Nuclear Recoil Theory

To understand the geometry setup of the IMPACT measurement and the importance of measuring the recoil angle of the neutrons, it is necessary to dive into the theory describing the scattering of neutrons. At its base, the interaction between the incoming neutron and the atoms in the crystal lattice of the detector is just an inelastic scattering, where part of the neutron energy is transferred to the lattice. This absorbed energy shows up in the detector in the form of phonon propagating through the lattice as well as ionization of charges.

As a consequence, calibrating the energy scale of the detector requires prior knowledge of the energy deposited by the neutron on the lattice. This is achieved by catching the neutrons behind the detector once they are scattered. As we will see, the outgoing angle of an elastically scattered neutron depends on the energy lost by the particle. Therefore, choosing a scattering angle corresponds to choosing an amount of energy deposited by the neutron on the detector.

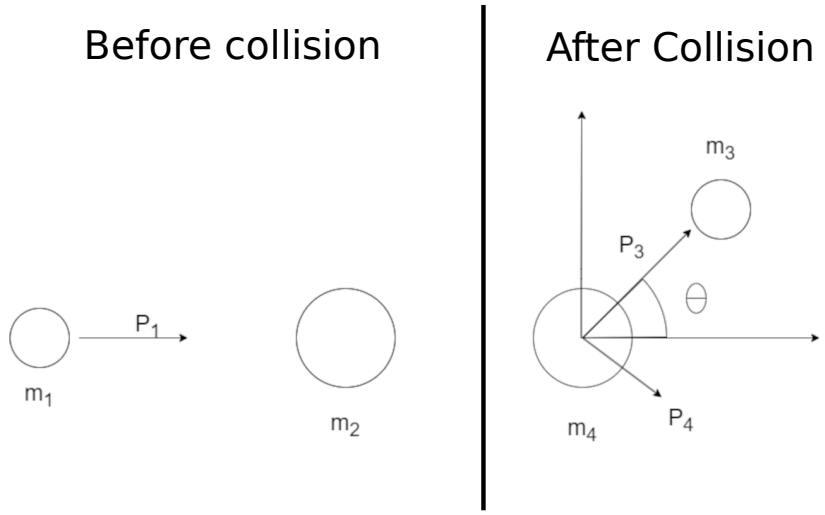

Figure 1.3. kinematics diagram for nuclear recoil.

We consider the interaction to be an elastic collision. One could consider the interaction to be inelastic, but it has been shown that, at KeV energies, the Migdal Effect is subdominant[**17**]. In this case, the incoming neutron with mass m_n and velocity V_n in the laboratory frame of reference. Similarly, the nuclei in the target lattice will be described by mass m_T and velocity V_T. We must note that, in the lab frame, the target nuclei are considered at rest. Now we consider the relativistic kinematics of the problem by applying energy and momentum conservation and the Q-value of the reaction. See figure 1.3.

Applying energy conservation, and recalling that the target nucleus is considered to be at rest ($E_2 = 0$), we have that:

$$(E_1 + m_1c^2) + m_2c^2 = (E_3 + m_3c^2) + (E_4 + m_4c^2) \tag{1.2.1}$$

Reworking this equation leads us to find an expression for the Q-value as follows:

$$E_3 + E_4 - E_1 = (m_1 + m_2 - m_3 - m_4)c^2 = Q \tag{1.2.2}$$

Looking at the conservation of linear momentum, we see that:

$$\overrightarrow{P_1} + 0 = \overrightarrow{P_3} + \overrightarrow{P_4} \Rightarrow \overrightarrow{P_4} = \overrightarrow{P_1} - \overrightarrow{P_3} \tag{1.2.3}$$

Letting θ be the scattering angle of the incoming particle, the magnitude of the nuclear recoil momentum is then:

$$P_4^2 = (\overrightarrow{P_1} - \overrightarrow{P_3})^2 = P_1^2 + P_3^2 - 2P_1P_3\cos\theta \tag{1.2.4}$$

Recalling that the kinetic energy can be written as $E_i = \frac{P_i^2}{2m_i}$. Therefore we can write the recoil energy E_4 as:

$$E_4 = \frac{P_4^2}{2m_4} = \frac{P_1^2}{2m_4} + \frac{P_3^2}{2m_4} - \frac{P_1P_3}{m_4}\cos\theta \tag{1.2.5}$$

Replacing the energies in 1.2.2 by the momentum expressions, we have that:

$$E_3 + E_4 - E_1 = \frac{P_3^2}{2m_3} + \frac{P_1^2}{2m_4} + \frac{P_3^2}{2m_4} - \frac{P_1P_3}{m_4}\cos\theta - \frac{P_1^2}{2m_1} = Q \tag{1.2.6}$$

Simplifying:

$$Q = \frac{P_3^2}{2m_3}\left(1 + \frac{m_3}{m_4}\right) + \frac{P_1^2}{2m_1}\left(\frac{m_1}{m_4} - 1\right) - \frac{P_1P_3}{m_4}\cos\theta \tag{1.2.7}$$

If we take this last expression and rework it in terms of energy we finally obtain:

$$Q = E_3\left(1 + \frac{m_3}{m_4}\right) - E_1\left(1 - \frac{m_1}{m_4}\right) - \frac{2\sqrt{m_1m_3E_1E_3}}{m_4}\cos\theta \tag{1.2.8}$$

At this point, it is convenient to look at the specific details of our problem. We know that the mass of the neutron appears as $m_1 = m_3 = m_n$ and the mass of the target nucleus shows up as $m_2 = m_4 = m_T$. Similarly, we have that the energy of the neutron before the recoil is $E_1 = E_n$, and its energy after the recoil is $E_3 = E'_n$. If we assume that the whole interaction was an elastic scattering so that $Q = 0$, the energy of the nuclear recoil is given by $E_4 = E_{nr} = E_n - E'_n$. With this setup, we can use the expression for Q to solve for E'_n in terms of E_n, to finally calculate E_{nr}.

As mentioned before, We solve for E'_n by setting 1.2.8 equal to zero and assuming that 1.2.8 is a quadratic equation such that $\sqrt{E'_n} = x$. We obtain:

$$x^2\left(1+\frac{m_n}{m_T}\right) - E_n\left(1-\frac{m_n}{m_T}\right) - \frac{2xm_n}{m_T}\sqrt{E_n}\cos\theta = 0 \tag{1.2.9}$$

$$x^2 - \frac{2m_n}{m_n+m_T}x\sqrt{E_n}\cos\theta - E_n\frac{m_T-m_n}{m_n+m_T} = 0 \tag{1.2.10}$$

We now just find the roots of the quadratic equation with $a = 1$, $b = \frac{2m_n}{m_n+m_T}\sqrt{E_n}\cos\theta$ and $c = E_n\frac{m_T-m_n}{m_n+m_T}$. This yields:

$$\sqrt{E'_n} = \frac{m_n}{m_n+m_T}\cos\theta\sqrt{E_n} \pm \frac{\sqrt{E_n}}{m_n+m_T}\left(m_n^2\cos^2\theta + m_T^2 - m_n^2\right)^{\frac{1}{2}} \tag{1.2.11}$$

Choosing the root with the positive sign so that $\sqrt{E'_n}$ has a physical result, we now just need to square this root and then perform the subtraction to calculate the recoil energy. In order to alleviate this work, the algebra for squaring and simplifying $\sqrt{E'_n}$ is left to the reader. One must obtain:

$$E'_n = \frac{E_n}{(m_n^2+m_T^2)}\left(m_n^2\left(2\cos^2\theta - 1\right) + m_T^2 + 2m_n^2\cos\theta\sqrt{\left(\frac{m_T}{m_n}\right)^2 - \sin^2\theta}\right) \tag{1.2.12}$$

The energy of the nuclear recoil is then:

$$E_{nr} = E_n - E'_n = E_n - \left(\frac{E_n}{(m_n^2+m_T^2)}\left(m_n^2\left(2\cos^2\theta - 1\right) + m_T^2 + 2m_n^2\cos\theta\sqrt{\left(\frac{m_T}{m_n}\right)^2 - \sin^2\theta}\right)\right) \tag{1.2.13}$$

Simplifying, we obtain:

$$E_{nr} = \frac{E_n}{(m_n^2+m_T^2)}\left((m_n+m_T)^2 - m_n^2\left(2\cos^2\theta - 1\right) - m_T^2 - 2m_n^2\cos\theta\sqrt{\left(\frac{m_T}{m_n}\right)^2 - \sin^2\theta}\right) \tag{1.2.14}$$

$$E_{nr} = \frac{2E_nm_n}{(m_n^2+m_T^2)}\left(m_n\sin^2\theta + m_T - m_n\cos\theta\sqrt{\left(\frac{m_T}{m_n}\right)^2 - \sin^2\theta}\right) \tag{1.2.15}$$

$$E_{nr} = \frac{2E_nm_n^2}{(m_n^2+m_T^2)}\left(\frac{m_T}{m_n} + \sin^2\theta - \cos\theta\sqrt{\left(\frac{m_T}{m_n}\right)^2 - \sin^2\theta}\right) \tag{1.2.16}$$

Equation 1.2.16 is our objective. It relates the energy of the nuclear recoil, that is, the energy picked up by the detector, to the initial kinetic of the neutron E_n and its recoil angle θ. Given that we have a nearly monochromatic neutron beam, equation 1.2.16 allows us to probe different recoil energies by looking at different recoil angles.

1.3. The Position Of the HVeV Detector

A deep understanding of the geometry of the experiment is necessary to achieve a low systematic error in the measurements. As seen in the previous section, the recoil energy that we choose to study is dependent on the recoil angle of the neutron. This measurement depends intrinsically on our understanding of the geometry of the experiment. An error in the alignment of the beam, the HVeV detector, or the backing neutron detectors will translate into a less reliable calibration of the detector. There are multiple things that could muddle the geometry; things such as the backing neutron detectors being displaced transversally or longitudinally, the position of the ADR fridge changing or the neutron collimator changing the direction of the incoming particles. However, most of these sources can be easily controlled or accounted for by keeping tight control of the experimental environment.

The one element that can be very challenging to account for is the position of the HVeV detector inside the cans of the ADR fridge. Recall that the detector must be cooled down to millikelvin temperatures. This means that in order to keep the detector's position fixed while it cools down, we need to take into consideration the thermal contraction of the different materials inside the refrigerator. Under normal circumstances, the thermal contraction is already accounted for in the design of the fridge, but given the importance of understanding the measured angle, we also need to consider any deviation from the detector's nominal position, even if it is very small. We must also account for the fact that the point of impact of the neutron on the detector crystal is unknown, which will also affect our measurement of the recoil angle. My work with the HVeV detector was focused on looking at ways to include this possible deviation through simulations of the IMPACT setup that can be performed anytime, and industrial radiography performed at any point during run time as long as the detector is kept operating temperatures. The next two sections will look at these lines of work.

1.3.1. Simulations: Independent Motion of the HVeV Detector Within the ADR

Given the wide range of possibilities from all the small-scale experiments, the SuperCDMS collaboration has also developed a simulation software based on the Geant4 libraries written in C++. The software, called SuperSim, uses version 10.7 of the Geant4 libraries and allows the user to choose the experiment, geometry, detector, particle beam, etc. It is designed as an Object Oriented software that gives high customization and allows the user to precisely simulate specific situations and geometries that could apply to all of the SuperCDMS experiments.

In the case of the IMPACT geometry, SuperSim builds up the detector geometry and then places the ADR at the center of its "world" space. However, The detector itself was

linked to the instantiation of the ADR object. Thus, moving the detector required moving the ADR fridge as well. This obviously does not allow us to investigate the possible offset of the HVeV detector from its nominal position. To solve this issue, I set out to investigate how does SuperSim build the ADR, so that I could, later on, modify the code to allow to independently move the HVeV detector within the cans, once the ADR is placed in the world.

After multiple attempts, I realized I could take advantage of the heavy reliance of SuperSim on object-oriented programming to move the detector after the whole ADR was placed in the simulation world. This way, the position of the HVeV detector can become a user-defined input, for which the default value is set to be its nominal position. This was done through additions to the `NWADR.cc` class, together with its corresponding header file. In addition, I created the `NWADRMessenger.cc` class and its header file to create a macro command allowing the user to input the desired offset for the detector's position.

More precisely, I modified the `NWADR.cc` class in order to turn the positions of the detector and its accompanying pieces a member of the class. This allowed me in turn to write the `NWADR::ApplyInnerOffset` method that introduces the desired detector offset, while also clearing out any previous offset so that the effects of this method do not pile up over repeated runs. Once this feature was tested, it was used in multiple simulations by the IMPACT

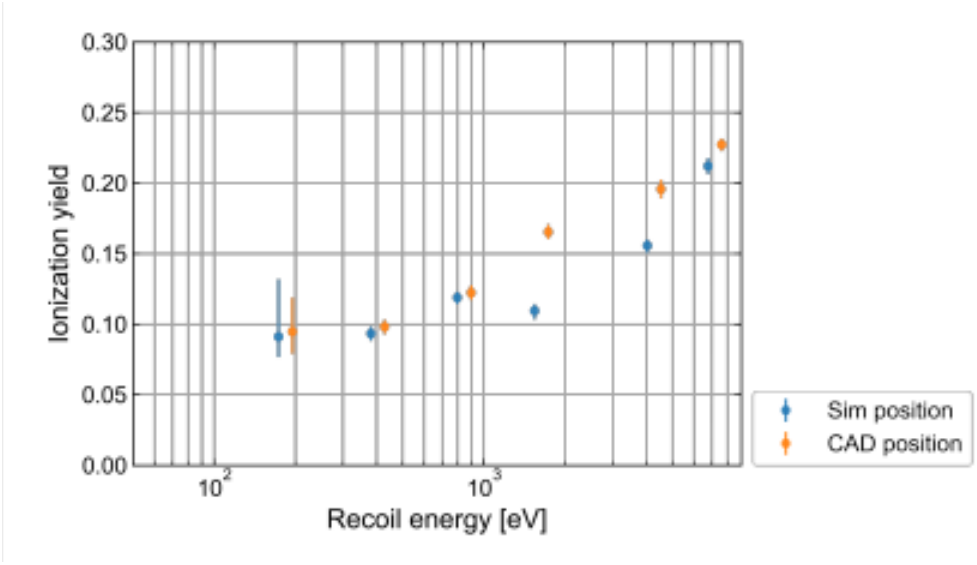

Figure 1.4. Ionization yield for Simulated and CAD positions

working group to account for the systematic error coming from the possible misalignment of the detector or neutron beam. As an example. Figure 1.4 shows us the resulting ionization yield at different recoil energies. This plot takes advantage of the independent motion of the HVeV detector to simulate the yield, supposing the detector is at 2 different positions. The CAD position corresponds to the detector position in the initial 3D drawings of the ADR, while the Sim position corresponds to the reconstructed position after the alignment with

a Cobalt-57 source was completed. The IMPACT group saw that the difference between the two detector positions in ring detectors is within statistical uncertainty. The biggest effect was seen on the set of detectors named "lone wolves". These detectors are part of the refrigerator itself and are therefore much more sensitive to any slight shift in the detector's position.

1.3.2. Industrial Radiography

1.3.2.1. Experimental Setup. On the experimental side, we needed to verify that the HVeV detector chip did effectively move during the fridge cooldown, and if so, by how much. To look at this problem, We set out to use the radioactive sources available at the lab to make a radiograph of the relative area where the detector should be. One of the best options available to us was to use the 400 ISO Kodak Industrex AA400 film. This film is widely used in industrial radiography settings as it provides high contrast, high speed, and fine-grain images. It is generally used in aerospace applications, archaeology, forensics, etc [**3**]. The film is sold in multiple formats, thus we chose the 17" × 4.5" version, as it was the more convenient size to work with. In order to obtain a visible image on the film, a minimum dose of 1 mSv was necessary. After running calculations regarding the type of radioactive source, its activity, and its distance to the film, we quickly realized that our best bet was a Caesium-137 (Cs-137) source with an activity at the time of 5 mCi and gamma energy of 661 keV. Given that the fridge has a radius of about 40 cm, we obtained a dose rate of about 0.088299 mSv/hr, meaning that the exposure time needed to be at least 11.3 hr.

Two rounds of exposure were made. For the first one, a film was placed between 2 lead screens with a thickness of 27 μm; this film was labeled with the number 1 on one of its corners. A second film was also placed behind the lead "sandwich", being labeled with the number 2. The ensemble was then placed in a sleeve, and then taped on the ADR. As a point of reference, a small piece of lead was taped to the side of the fridge. This piece not only provides a guide as to what area should the film cover, but it also will serve as a size reference for the final image. Diametrically opposite to the film, the rod containing the Cs-137 was placed so that its tip made contact with the wall of the refrigerator. The total exposure time for this round was 13.22 hr. The second round of exposure had a duration of 16.83 hr. This time, a single film was used inside the lead screens and placed in the sleeve; this film was therefore labeled as number 3.

It must be noted that the use of the Cs-137 source is less than ideal, but was the best option available at the moment. Figures 1.5 and 1.6 clearly have a very low density. For future runs, the use of a proper x-ray source will prove useful as it can be tuned to have a much lower attenuation and higher intensity. Let us calculate the total attenuation factor μ_{total} for a given gamma energy through a given material thickness. We have then $\mu_{total} = \mu_m \rho L$,

	Cs-137 source (661 keV)			
	Total cross section [barns]	Mass attenuation coefficient [cm^2/g]	Transmission through the material	Transmission through both materials
Aluminum (1.2 cm)	3.333	0.07438	0.2142	0.02487
Niobium (0.2 cm)	11.12	0.07203	0.1161	

	X-ray source (100 keV)			
	Total cross section [barns]	Mass Attenuation Coefficient [cm^2/g]	Transmission through the material	Transmission through both materials
Aluminum (1.2 cm)	7.043	0.1572	0.3991	0.3223
Niobium (0.2 mm)	148.34	0.9615	0.8076	

Table 1.1. Calculated transmissions through the materials

where μ_m is the mass attenuation coefficient in cm^2/g, ρ is the mass density of the material in g/cm^3, and L is the material thickness in cm. The transmission through the material is given by $t_i = 1 - e^{-\mu_{total_1}}$, and the transmission through multiple materials is the product $t_{total} = t_1 \times t_2 \times ....$ In our case, the photons must go through multiple cans surrounding the detector; they total 1.2 cm of Aluminum and 0.2 cm of Niobium. The calculations are summarized in table 1.1 using data from the *XCOM* database[**2**], and assuming an X-ray source capable of producing 100 keV gammas. The advantage of using such a source is clearly seen when considering a much higher intensity. Given the initial activity of the Cs-137 source and the distance to the film, the calculated dose-rate of 0.01780 mSv/hr is brought down to 0.0004427 mSv/hr. Assuming the X-ray source can produce a dose rate of 1 mSv/hr, the intensity arriving at the film would be about 0.3223 mSv/hr. Considering a 1 mSv dose to obtain the desired image density, the Cs-137 source would require an exposure of over 2200 hours, while the X-ray source would achieve the same density with an exposure only 3.103 hours long. The use of such an X-ray source will also provide better contrast in the film because there is a larger difference in the transmission coefficients with 100 keV gammas, as seen in table 1.1.

1.3.2.2. Film Processing. The films were developed in the university's darkroom with the help of a photography technician. Using methods from black and white film photography, films 1 and 2 were developed with the Kodak D-76 developer for about 5 minutes. They were then treated with a 30 seconds stop bath and a 3 minutes fixation bath. At the naked eye, very few details were visible in these two films (See figure 1.5); therefore a different strategy

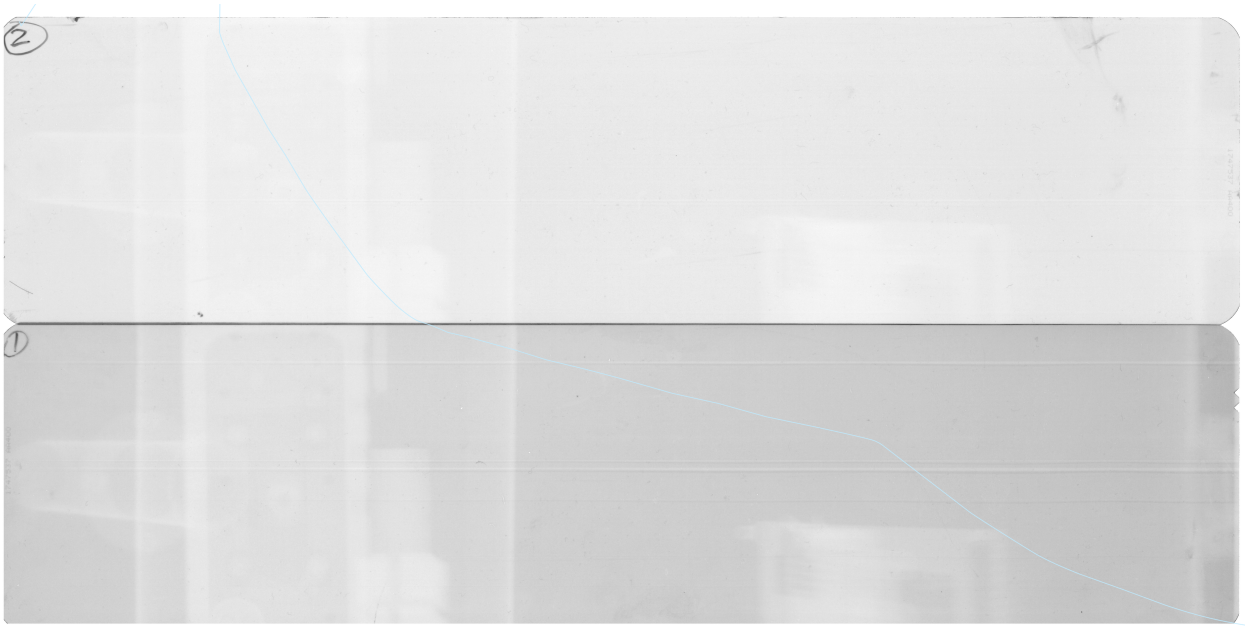

Figure 1.5. Scanned Image of films 1 and 2

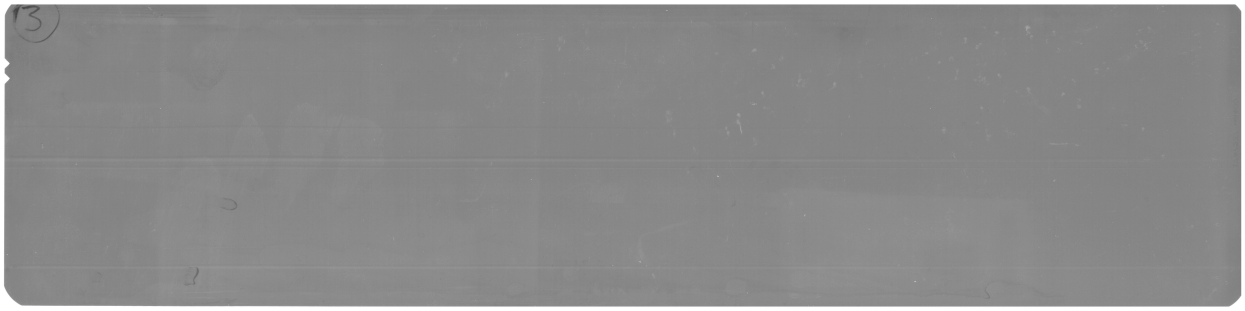

Figure 1.6. Scanned Image of film 3

was used for the third film, with the objective of ruling out problems with the developing agent or time. For this last film, we used the Kodak Tmax developer, pushing the developing time to 8 minutes, and keeping the stop bath and fixation bath at 30 seconds and 3 minutes respectively. This last film came out to be much darker and the details of the image were much easier to see to the naked eye (See figure 1.6).

The scanned images allowed for further processing with the help of editing software in order to enhance the contrast of the image. The objective of using this film is measuring the size of the features, and knowing the dimensions and the position of the film with respect to the source, we were capable of reconstructing the original position of the detector. Figure 1.7 shows the enhanced image of film 1 and the measurements taken on it. These last were obtained by making an equivalence between the length of the film on the image, in pixels, and the physical length of the film in millimeters. The scale was also verified with the lead piece and the average came down to 0.085662 mm/pixel.

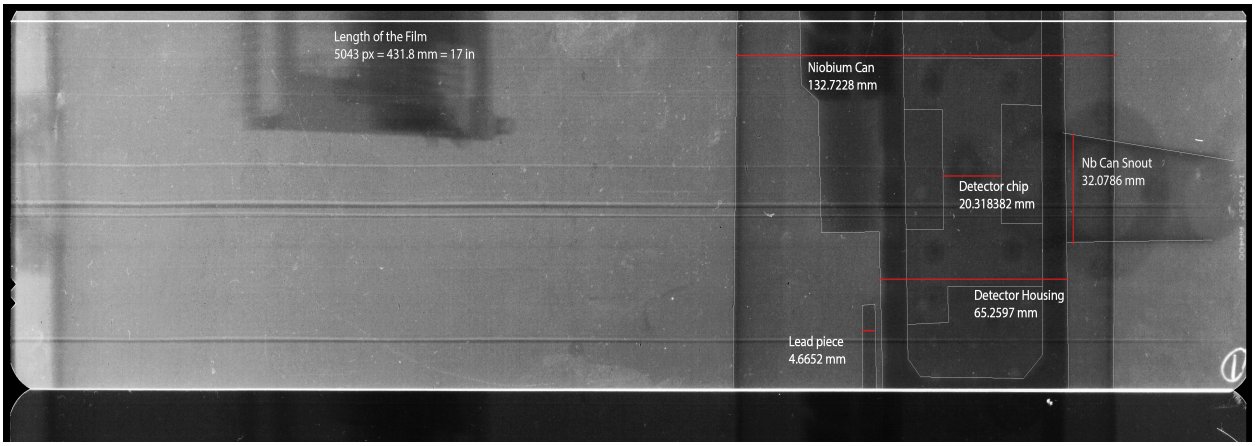

Figure 1.7. Enhanced image of film 1

1.3.2.3. Position reconstruction. The size measurements taken from the film allowed us to reconstruct the position of the HVeV detector. In fact, given that the position of the Cs-137 source with respect to the film and the fridge was known, I was able to produce a diagram that showed the reconstructed position of the detector. The radiograph was taken with the detector and the beam at the 15° position, so the diagram was pretty straightforward. Once the fridge, the radioactive source, and the film were drawn at their corresponding positions and with their corresponding sizes, one simply had to extend projection lines from the source to the features seen on the film, keeping in mind the 15° rotation. For example, extending two lines from the Cs-137 source to the edges of the detector housing seen in the film. Next, knowing the horizontal dimensions of the given element, I drew a horizontal line of the same dimension that connected the two projection lines. This way, the position of the horizontal line with respect to the drawing of the fridge will correspond to the physical position of that element inside the ADR. As a reference feature, I chose the detector housing, as it is very easy to pick up from figure 1.7, and physically close to the actual Silicon crystal used in the detector. Figures 1.8 and 1.9 show the results of the reconstruction diagrams. Here, the solid lines show the projections of the edges of the radiographic film, while the dashed lines correspond to the projections from the detector housing. One remark about this reconstruction diagram is the fact that it completely ignores the dimensions in the Z-axis. This was possible given that the figure 1.7 shows the silicon chip pretty much at its center, effectively simplifying the problem from one in 3 dimensions to one in 2 dimensions.

When comparing the results of the diagram with the CAD drawings of the fridge, one can quickly conclude that the detector position stayed pretty much the same, considering an error margin. In fact, if I assume a 15° clockwise rotation, one concludes that there is a small mismatch between the reconstructed position and the CAD position, as shown in the close-up depicted in figure 1.10. to compare these two positions, a line was drawn between the center of the lines representing the detector housing. For figure 1.10, the graph

shows a distance of 2.516 cm. If we now consider an error in the measurements of the Cs-137 source, the position of the fridge with respect to the source, or the size of the rotation itself, a conservative estimate could be summed up into a $\pm 5^\circ$ in the rotation. That is

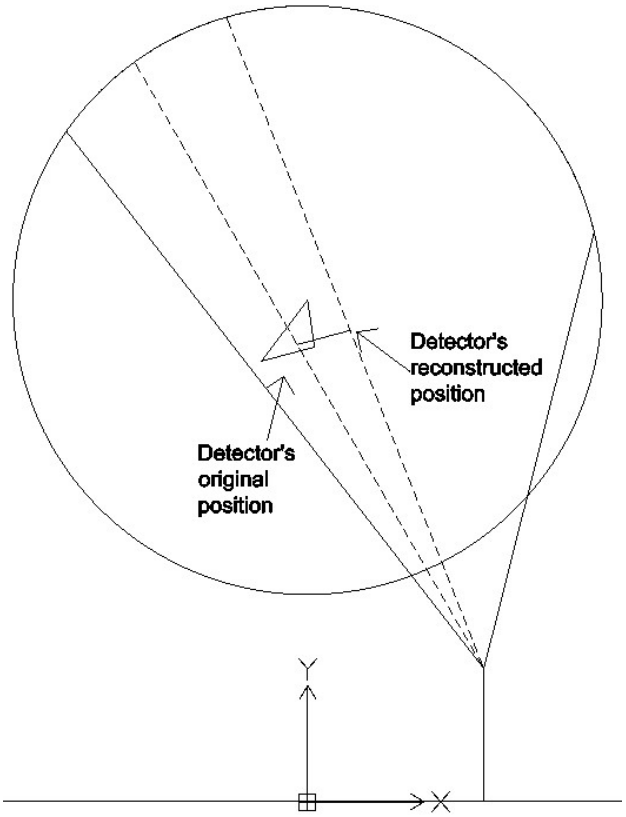

Figure 1.8. Reconstruction diagram for a 15° rotation.

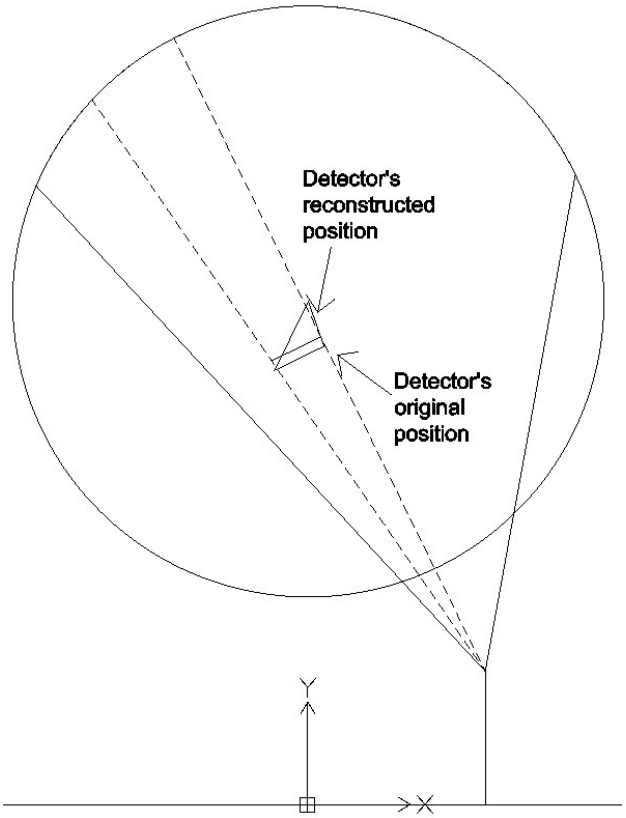

Figure 1.9. Reconstruction diagram for a 19° rotation.

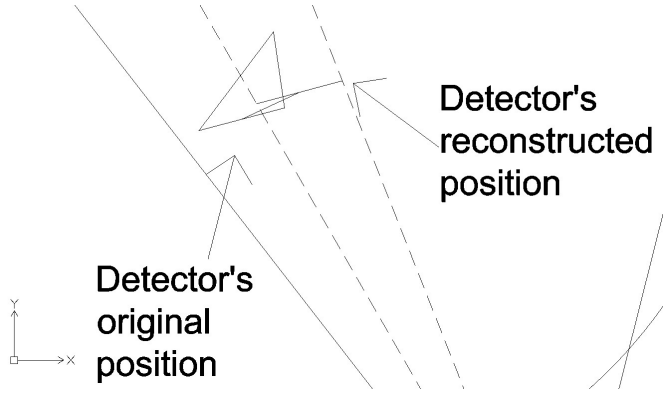

Figure 1.10. Close-up on the reconstruction diagram for a 15° rotation.

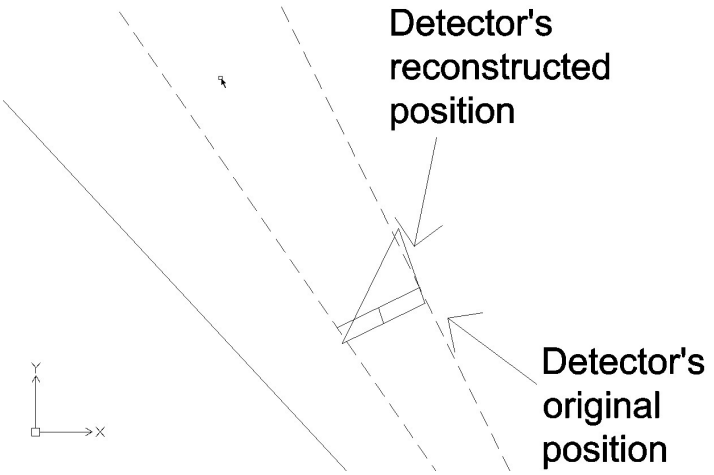

Figure 1.11. Close-up on the reconstruction diagram for a 19° rotation.

why I also investigated a rotation of 18°, 19°, and 20°, as going under 15° would only increase the distance between the reconstructed and the CAD position. As it turns out, a rotation of about 19° produces the closest reconstruction, given that with a 20° rotation, the distance between the positions starts to grow again. Figure 1.11 shows then a close-up of the best reconstruction diagram. This corresponds to a 19° rotation, which yields a separation of 0.636 cm between the positions. I must note that no values between 19° and 20° were tested due to limitations from the software used to make the diagrams. Nonetheless, one can safely say that the detector's position changed by at most 6 mm. In short, the industrial radiography work leads us to conclude that the shift in detector position is small in comparison to the detector's size. As a consequence, the uncertainty linked to the detector's position is well accounted for by systematic uncertainties in the TUNL measurement and can be directly measured in future calibration experiments at Montreal.

Chapter 2

Implementation of an Importance Sampling Algorithm in the Context of the Simulations Software SuperSim

2.1. Variance Reduction in Monte Carlo Simulations

Markov Chain Monte Carlo (MCMC) simulations are a very powerful tool in computational physics. However, this technique can be very computationally expensive when trying to simulate complex, real-world, experiments. To deal with this issue, different shortcuts have been devised and are known under the umbrella term "Variance reduction techniques". These methods aim to decrease the computational cost, while still producing realistic and statistically significant simulations of physical processes. The choice of these clever tricks will depend on the specific details of the simulation at hand, but in the end, they modify the simulation process itself or simplify the physics models used. In the context of the SuperCDMS collaboration, I worked toward integrating the importance sampling, or importance biasing method, for the lead shield of the SNOLAB configuration.

When simulating particle physics, the MCMC methods try to approach the expectation value $\langle x \rangle$ of a probability distribution $p(x)$ by looking at the mean $\bar{x}$ of a discrete distribution of particles after they undergo the pertinent physical processes. More explicitly, $\langle x \rangle$ is the true mean of the distribution $p(x)$, and as such, we would need to throw infinitely many simulated particles to obtain this value. The MCMC methods try to approach $\langle x \rangle$ through $\bar{x}$, which is the mean of an arbitrary subset of this infinite simulation. For a set of N recorded particles, the mean is given by:

$$\bar{x} \equiv \frac{1}{N} \sum_{i=1}^{N} x_i \tag{2.1.1}$$

Consequently, the standard deviation S^2 of this discrete distribution is given by:

$$S^2 \equiv \frac{1}{N-1}\sum_{i=1}^{N}(x_i - \bar{x})^2 \tag{2.1.2}$$

Now, given the law of large numbers, we are ensured that $\langle x \rangle \to \bar{x}$, as long as $\langle x \rangle$ is a finite number. The use of a large enough N also allows us to approximate the standard deviation with $S^2 \approx \overline{x^2} - \overline{x}^2$, where $\overline{x^2} = \frac{1}{N}\sum_{i=1}^{N} x_i^2$. The variance on the mean $\bar{x}$ is therefore:

$$S_{\bar{x}}^2 = \frac{1}{N}S^2 \tag{2.1.3}$$

Taking advantage of the central limit theorem, we can repeat the simulation multiple times, each with N recorded particles, and we will see the mean $\bar{x}$ of each simulation will follow a normal distribution around the true mean $\langle x \rangle$, with variance $S_{\bar{x}}^2$. Here is where we see the effects of the variance reduction workarounds. In a simulation with multiple runs and without variance reduction, we will see that all the $\bar{x}$ measured in each run has a given spread around the true mean $\langle x \rangle$. In comparison, a similar simulation with multiple runs but with variance reduction methods will see the $\bar{x}$ will have a smaller spread around the true mean $\langle x \rangle$. In other words, these techniques try to concentrate all the estimations of the mean, that is $\bar{x}$, around the true mean $\langle x \rangle$, effectively decreasing their spread $S_{\bar{x}}^2$ around $\langle x \rangle$. Hence, compared to a direct simulation, we require fewer runs to produce the same level of confidence in the result, reducing the computation expense to obtain the said result.

Specifically, in the SuperCDMS case, the distribution we want to measure is the energy spectrum of scattered radiation in a single detector, and any correlations between energy deposited in multiple detectors. Thus, our random variable x is a large multi-dimensional probability density, with one dimension per detector channel, and the energy in that detector as the independent variable. My work was focused on simulations through a part of the SNOLAB shield. The low survivability of this area allows us to assume that the off-diagonal elements are unaffected when propagating through this volume. In other words, the probability that a single primary particle would physically produce two different particles that survive the propagation through the shield and hit the detectors is low. This assumption allows the random variable x to be factorized by re-throwing particles inwards.

The expected mean for this distribution has a minuscule positive value for any given bin in the array. Thus, variance reduction for us will simulate fewer zero-hit contributions while reducing the weight of simulated hits, to bring them closer to the mean. On top of this, Variance reduction will use binning to approximate the continuous distribution of deposited energy around the simulated value. Other techniques, in particular the Boltzmann equation, can be used to calculate the average radiation field, and thus completely reduce the variance on diagonal elements of the random variable x. However, this equation does not permit the preservation of temporal resolution, and hence, the correlated energy depositions amongst

detectors that we require are also lost. The loss of correlation information is the greatest weakness of variance reduction techniques.

2.1.1. Importance Biasing in Geant4

The importance sampling method is one of the workarounds that modify the simulation itself. It uses a geometric approach to control the population of particles to solve the variance reduction problem. This method also allows the user to tailor the algorithm by deciding the type of particle and on which volumes it happens, making it robust and easy to use. Conceptually, the importance biasing process is set up as follows. The region of interest is virtually subdivided into contiguous cells, called importance cells. Note that these divisions only concern the chosen particle type. All other particles will never encounter these boundaries and the result of their simulation remains unchanged. Another feature of this technique is that the biasing volume, the space on which importance biasing is being applied, is completely arbitrary. This volume does not necessarily need to match the boundaries of the different components of the experiment being simulated; all it needs is to be contained in the world volume of the simulation. With the biasing volume and its cells defined, an importance weight is assigned to each of the subdivisions. As a general consideration, it is recommended to assign the weights such that the biggest one is closer to the point where the particles will be recorded. From this point on, the recording surface or volume will be commonly referred to as the "scorer". This completes the geometric setup of the importance method.

Next, population control is accomplished by adding two processes to the pre-existing physics model; these are Geometric splitting and Russian Roulette. These two processes will either split the particle while also changing its own weight, transmit the particle while changing the particle's weight as well, or kill the particle altogether. These processes kick in when a particle reaches the boundary between 2 importance cells. the criteria to decide exactly what happens to the particles, and how it is done, depends solely on the ratio of importance weights of the 2 cells involved.

Summing up the effects of the 2 processes, we see that the biased particle's population increases in a given direction, making it more likely that they will hit the scorer at our interest point. This increased number of counts is counteracted by having the particle's weight modified. In a way, importance sampling is considering the different paths that a particle could take on its way to the scorer, such that the weight of the particle recorded at this point is a representation of the likelihood of a given trajectory.

2.1.1.1. The Algorithm. In order to understand better the behavior of these population control processes, let us follow the trajectory of a biased particle, with initial weight w_init, inside the biased volume. Following the notation used in the Geant4 documentation, the

importance cell where the particle starts will have the importance weight *ipre*. The following importance cell will then have the *ipost* weight assigned. When a particle reaches the boundary, the simulation will check these two values and calculate their ratio $r = \frac{ipost}{ipre}$. There are 3 possibilities considered for this value. If $r = 1$, none of the processes are applied and the particle is just allowed to continue its path. If $r > 1$, the particle gets to be split into r new particles, each with a new weight $w\_new = w\_init * \frac{1}{r}$., and effectively increasing the sampling rate of this specific particle type. Note that splitting the original track into r new ones implies that the ratio r should be an integer value, but depending on how the importance weights were attributed, this could not be the case. In the instance where r is not equal to an integer number, the quantity of new particles is set to the integer part of r, noted as $int(r)$, or it can be set to $int(r) + 1$; each option has a probability of occurring given by $1 + int(r) - r$, and $r - int(r)$ respectively.

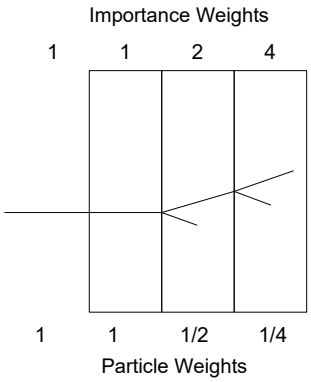

Figure 2.1. Splitting routine applied at the boundaries between 2 cells.

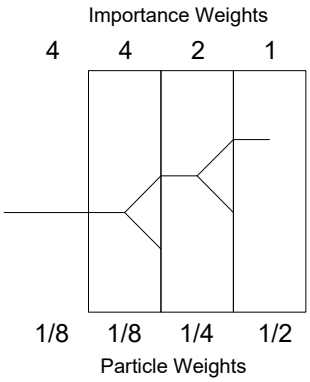

Figure 2.2. Russian Roulette routine applied at the boundaries between 2 cells.

Returning to the possible values of r, if $r < 1$, then the particle undergoes the Russian Roulette routine. As its name suggests, this process can kill the particle, with a probability of $1 - r$. In the given case that the particle is not killed, it gets a new weight given by $w\_new = w\_init * \frac{1}{r}$ again, and it is transported into the following importance cell. Figures 2.1 and 2.2 illustrate these two population control effects. Note that the splitting shown in figure 2.2 is meant to represent all other possible interactions the particle can have on its way to the boundary.

2.2. Importance Sampling Implementation in SuperSim

Given the multiple experiments that SuperCDMS is involved in, it is no surprise to see many modeled geometries in the SuperSim software. This, coupled with the fact that the importance biasing technique depends on the simulated geometry as well, made a general implementation of this variance reduction method a big task that could last a few years of

development. Therefore, it was decided to first implement it for a specific geometry where the increased sampling would be most helpful. The conclusion was then to implement Importance biasing on a component of the layered shield used in the SNOLAB configuration. This is one of the large-scale experiments being performed underground, making the cavern's natural radioactivity an important source of background noise for the multiple detectors. Trying to minimize the signals coming from gamma and beta radiation in the cavern, a 20 cm thick shield made of low-activity lead is used. It is on this specific layer that importance biasing has been implemented. This shield is not a monolithic piece, as it must be pierced at two different spots to allow the passage of the stems, i.e. the pipes carrying the cryogenic fluids and the electronics to and from the detector towers.

The final goal of implementing importance biasing in the lead shield is to better sample all the physical processes that the photons experience in the lead shield. These gamma particles have multiple sources, but they are the result of the decay of radioactive elements, and as such, are also considered a source of background noise for the detectors. The main sources of the photons are the decay chains of ^{238}U, ^{232}Th, and ^{40}K. These starting elements can be present as airborne dust that could accumulate directly onto the surfaces at different stages, be present in the cavern's rock itself, or be found as radioactive impurities inside the detector's materials[**1**]. Additional isotopes such as ^{46}Sc, ^{48}V, ^{54}Mn, $^{56-58}$Co, ^{59}Fe and ^{60}Co can be generated by cosmic activation of copper elements of the construction[**1**], and will also produce gamma photons in their decay. The photons that manage to reach the shield can undergo photoabsorption, pair production, or Compton scattering. In the case of photoabsorption, an atomic electron absorbs all the energy from the photon and is ionized. As the electron propagates through the material, it can produce other gammas by bremsstrahlung or annihilation. When pair production occurs, the original photon splits its energy by producing an electron and a positron. As before, these particles will emit bremsstrahlung photons or annihilate with the antiparticles in the vicinity. Finally, in a Compton scatter, the photon scatters off an electron, transferring part of its energy to the electron in the interaction. This process is the most concerning one, as a gamma with sufficiently high energy could suffer multiple Compton scatters and make its way through the lead shield, finally contributing to the background noise at the detectors. Effectively, figure 2.3 from the projected sensitivity of SNOLAB[**1**], shows that gamma and beta interactions are among the main sources of background noise. The effects of these types of interactions inside lead can be condensed into a single numerical value: the total mean free path of a photon in lead λ_{mfp}. Given the mass attenuation factor for a given energy μ_m and the mass density of the material ρ_m, the mean free path, in units of cm, is simply $\lambda_{mfp} = \frac{1}{\mu_m \rho_m}$. This value depends on the energy of the photons; as an example, the 0.511 MeV photons produced in the e^+-e^- annihilation have $\lambda_{mfp} = 0.607$ cm, while the 1.460 MeV gammas produced by the ^{40}K decays have $\lambda_{mfp} = 1.71$ cm. Therefore, a better understanding of the

physics happening inside the lead shield will help the collaboration to better understand the background signals. In the context of the final science goals, the use of importance sampling can improve our understanding of the lead shield and its effectiveness at blocking multiple sources of background noise.

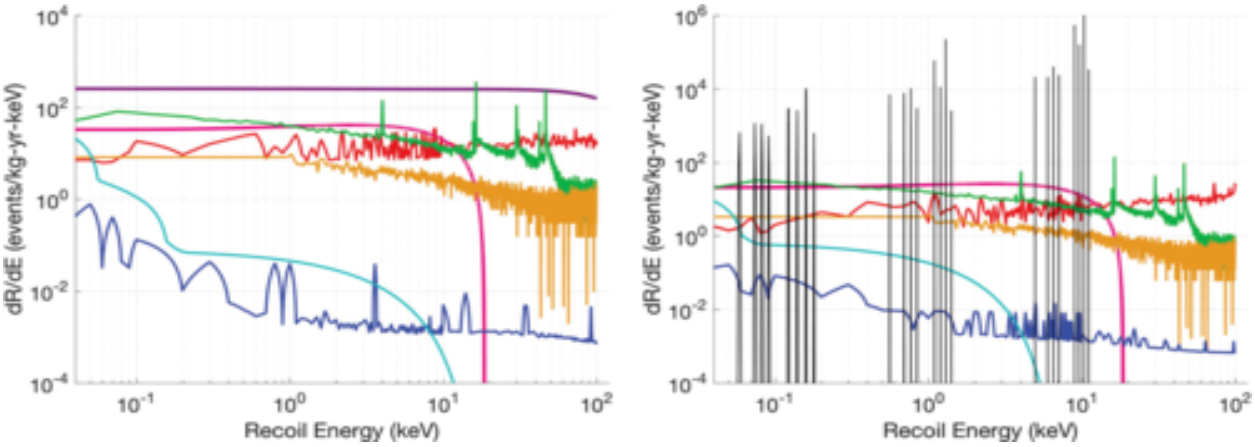

Figure 2.3. Raw background spectra of single-scatter interactions in a Si (left) and Ge (right) detector obtained from the MCMC simulation. The spectra are broken down into components and shown as functions of recoil energy (Electron Recoil or Nuclear Recoil depending on the interaction).^{3}H (pink) and ^{32}Si (purple) are the largest individual contributors to the backgrounds in the Ge and Si detectors, respectively. The remaining components are Compton scatters from gamma rays (red), surface betas (green), surface ^{206}Pb recoils (orange), neutrons (blue),‘ and coherent elastic neutrino-nucleus scattering (cyan). Note that the neutron spectrum (blue) has some spurious structure from the limited simulation statistics in the cavern component of the neutron background. Figure taken from [**1**]

It must be mentioned that the implementation task could be divided into two tasks; one concerning the geometry and the other concerning the physics lists. Robert Calkins contributed greatly to the setup of the geometry side, while I worked on both parts. As a general rule of thumb, the SuperCDMS collaboration has developed the SuperSim software to be executed in both single-threaded and multi-threaded modes. Nonetheless, the implementation of importance sampling is exclusive to the single-thread version, as the base libraries from Geant4 are not capable of operating multi-threaded when using importance sampling. This is considered to be a bug and not a feature of the Geant4 libraries, which has been duly reported to their development team.

2.2.1. The Geometry

Figure 2.4 shows the complete view of the SNOLAB geometry, as well as the layers that we are most interested in. The outer section is the Radon Barrier, where the primaries originate in the simulation, the middle section represents the lead shield itself, and the inner section depicts the Inner Poly. The lead shield of the SNOLAB configuration is modeled

as a 20 cm thick cylindrical shell made out of lead. The creation of the importance cells is operated in a parallel world created exclusively for the importance biasing processes; this world is named `BiasingWorld`. The creation of the parallel world is due to the class `CDMSParallelWorld.cc`, while the construction of the importance layers happens in the class `CDMSGeomConstructor.cc`. Although important, these two classes only ensure that the importance cells are created in the correct volume and at the right time within the structure of the software. The actual definition of these cells happens within the class `CDMSCylinderLayer.cc`, with the `CDMSCylinderLayer::BuildImportanceLayers` method. This class was used to create concentric cylindrical shells of a given length and assigned them the importance weights as powers of 2, with the *nth* layer having the weight 2^n. At the same time, these layers were registered in the `G4IStore` class, which is the way GEANT4 uses to track all the information about the importance cells and their weights. Using simple cylindrical layers allows to simplify the creation of these geometric volumes and also ensures a similar sampling behaviour in the case where a particle escapes from the lead shield into one of the stems, or vice-versa.

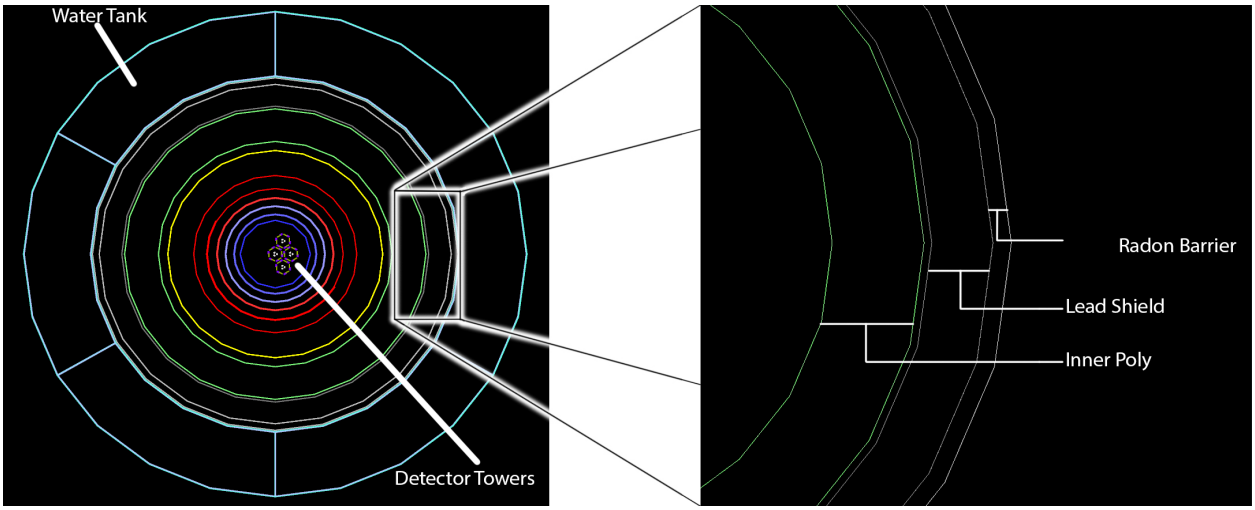

Figure 2.4. Top view from the SNOLAB geometry and an enlarged view of the layers of interest

The choice of importance weights as powers 2^n seemed the most sensible as it would keep a constant ratio between the weights of contiguous cells. Indeed, this ratio is 2 for the splitting case, which halved the particle weights and produce 2 traces from every single one that made it to the boundary between cells. In the case of Russian Roulette, the ratio is maintained at 0.5, giving the particle a 50/50 chance of being killed or having its weight doubled. An important limitation of the important weights is due to the data type used to define them, as they are stored as integer values. Being a 32-bit variable, its theoretical maximum value is $2^{31}-1$, but it can be less as this limit is compiler-dependent. This imposes a theoretical limit on the number of importance cells at 31 layers. On the other hand, using

such a high number of cells could quickly oversample the gamma particles as well as slow down the whole simulation, which defeats the purpose of a decreased computational expense. Thus, the choice of the number of cells is left to the user as a tunable parameter to be tailored for the desired simulation.

The number of layers is set through a macro command added to the `CDMSCylinderMessenger.cc` class. This command requires a length input in units of cm, as it is easier to create the importance cells from a fixed length, called importance length. The use of an importance length also allows us to easily solve any issue that could come up from using a number of importance cells that do not fit exactly within the bigger importance volume. The way it is currently handled, the first $n-1$ layers are set to have the desired importance length, while layer n, the very last one, is extended all the way to the origin of the world. This feature is also designed to take the most advantage of the splitting algorithm, as this ensures that not many particles will be killed before arriving at the scorer, which would be placed inside the last importance cell. A different method was tried, where the importance cells were limited to the volume of the lead shield itself. In this case, if the number of importance cells did not fit, the code was designed to fill up the first importance cells, leaving the last layer to have the length of whatever space is left. This option was discarded nonetheless, as it killed a big number of particles when they left the importance volume. As a way to deal with the first transportation from the outside world into the importance volume, the importance store also assigns an importance weight of 1 to this outside world, keeping $r = 1$ when moving from the outside into the importance volume. In the case where the particle moves from the very last importance layer into the outside, the ratio r will always be less than unity, which would activate the Russian Roulette with a kill probability that gets higher and higher with an increasing number of importance cells. To illustrate, using 10 cells yields a kill probability of about 99.902%, while using 20 layers would virtually kill all particles, as the survival probability would be of about 9.5367×10^{-7}; this is a waste of computing resources as a particle being simulated through all of the importance layers in the shield would just be killed before being recorded by the scorer.

The number of importance cells is totally arbitrary for the user. However, this parameter is crucial in the production of accurate simulations. On one hand, using a large number of layers will oversample the particles, slow down the simulation and require more memory. The oversampling can also overestimate the results of the simulation, as it can push the mean measured by the simulation, $\bar{x}$, away from the true mean $\langle x \rangle$. On the other hand, too few layers can undersample some of the gammas, or have very little effect on the final result. The limiting case would be to choose the length of the shield as the importance length; effectively producing a single importance cell, equivalent to an unbiased simulation. The two extreme cases, oversampling and undersampling, will defeat the variance reduction

objective of importance sampling. A good rule of thumb would be to match the importance length to the mean free path λ_{mfp} of the simulated photons, but this idea may be problematic when dealing with multiple gamma energies, as it may undersample the photons with λ_{mfp} much smaller than the chosen importance length.

2.2.2. The Physics List

The implementation of the physics list takes care of adding the specialized importance process to the existing list. This can be very tricky as the base libraries from GEANT4 are very strict on what needs to be set up before adding the processes concerning the variance reduction techniques. In our case, the Geant4 documentation [**9**] clearly indicates that the `Configure` function can only be called once the `G4RunManager` has been initialized. This was executed through the newly created `CDMSImportancePhysics.cc`. This class follows a structure similar to the other specialized physics lists used in the SuperSim software, where the use of the overloaded `CDMSImportancePhysics::ConstructProcess` method is called with the other CDMS-specific physics list. Overloading the `ConstructProcess` function easily accomplishes two things: it ensures that the `G4RunManager` is already initialized so that the `Configure` function can be called on, as well as making sure that the process is not added too late in the stack of the software since the `Configure` method would be ignored if called too late. To complement the base structure of an additional physics list class, the `CDMSImportancePhysics::ConstructParticle` was also added. This method does not contribute to the functioning of importance sampling since this variance reduction method does not require the creation of new particles specific to the physics list. Hence, this function was used as a sanity check that will only return if there is no instantiation of a class defining gamma particles.

Another feature was created to allow the user to easily switch on or off the code pertaining to importance biasing. This was done through a macro command included in the `CDMSPhysListMessenger.cc`, which turns on or off a flag in the `CDMSPhysListFactory.cc` class. Consequently, the inclusion of the simple command `/CDMS/Physics/ActivateImportanceBiasing` tells the physics list constructor to also include the `CDMSImportancePhysics` class in its works. Even if the macro includes the creation of an importance volume with its importance cells, the absence of this macro command would not trigger the importance sampling functions. This feature is most useful in the context of running SuperSim interactively. It must be noted that a specific CDMS application, named `CDMS_ImpSamp`, was created to run all importance features during its development.

2.2.3. Validation Study of the Implementation

2.2.3.1. The Initial Conditions. After importance sampling for gamma particles in the lead shield was integrated into the code, a large-scale study was performed to ensure the results of the biased simulations were physically meaningful, and to compare it against an unbiased simulation with equal initial conditions. This study was executed at the Cedar cluster from the Compute Canada facilities with the following conditions: the biased simulation uses a set of 10 runs, each with 1×10^6 primary particles, for a total of 1×10^7 primaries. Taking into consideration the expected lower counts for the unbiased simulations, a total of 1×10^8 primaries was divided into a set of 10 runs, each with 1×10^7 particles. In both cases, the gamma particles originate from the Radon barrier, one of the inner layers of the shield structure. The scoring surface is then placed on the inner polyethylene layer, shortened to the inner poly. Therefore, if one moves inwards in our area of interest, the first layer seen is the radon barrier, followed by the lead shield, and finally, the inner poly will be found. The gamma photons are given an energy of 2 MeV and are limited to originate from a ring with a skin depth of 1 μm. This ring is centered on the x-y plane and extends 10 cm above and below this plane. The particles are set to have a momentum vector pointing inwards and they are given a half angle around the emission cone of 10°.

For the biased simulation, it was decided to use 16 layers, each with a thickness of 1.25 cm. This produces importance cells of the same size all throughout the lead shield, which ensures an equal probability for all the other processes that could occur between the boundaries of the importance cells. Another advantage of using an importance length of 1.25 cm is the fact that a bit more than half the particles will manage to get to be split at this length. Indeed, the half intensity length, $\chi_{\frac{1}{2}}$, given by $\chi_{\frac{1}{2}} = \frac{ln(2)}{\mu_m}$, where μ_m is the mass attenuation coefficient, in cm^2/g. At 2 MeV, we have that $\frac{\mu_m}{\rho} = 4.606^{-2}$ cm^2/g [**12**], where $\rho = 11.34$ g/cm^3 is the density of the material. Hence, the calculation of the half-intensity length is:

$$\chi_{\frac{1}{2}} = \frac{ln(2)}{\frac{\mu_m}{\rho}\rho} \approx \frac{0.693}{4.606^{-2} \times 11.34} \approx 1.33cm \tag{2.2.1}$$

With the half length of lead being about 1.33 cm and the importance length being slightly shorter, at 1.25 cm, we increase the number of particles that can make it through the lead shield.

The last element to consider in this validation study is the fact that the scorer was used in the spectrum counter mode. As a way of eliminating the particles that can scatter back from the inner poly, enter the lead shield and scatter back again into the inner poly, the spectrum counter kills the particles as soon as they are recorded. This not only helps to focus our analysis on the effects of the importance sampling methods, but it also reduces the

computational expense as the particles are only simulated in our region of interest and not propagated into regions that have no effect on the final results.

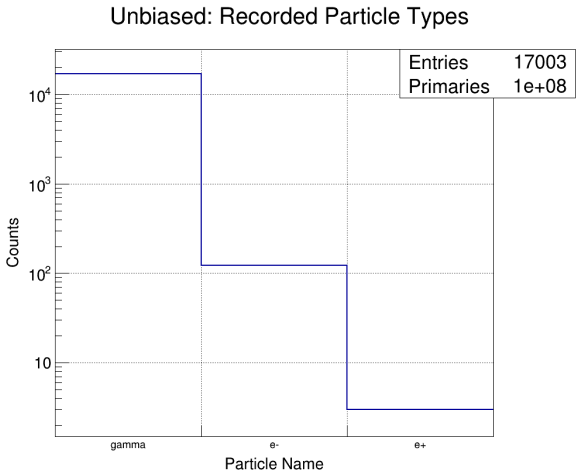

Figure 2.5. Histogram of the particle types recorded at the inner poly in the unbiased simulation.

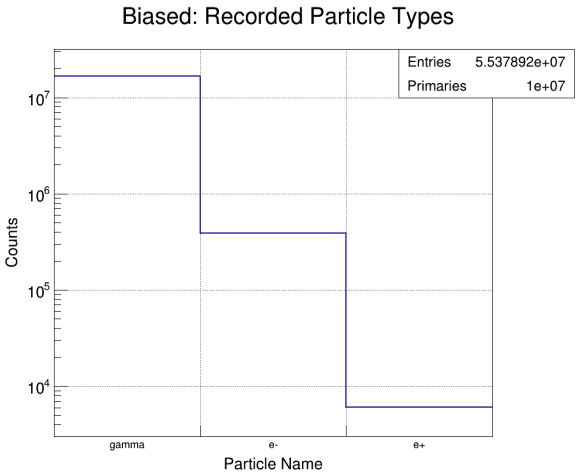

Figure 2.6. Histogram of the particle types recorded at the inner poly in the biased simulation.

2.2.3.2. Results and discussion. Three main histograms were produced to see the performance of the simulations. The first one simply counts the number of particles, separated by their types. This histogram is useful in the first instance as it paints a clear picture of the type of particles generated by the interaction between the primary particles and the lead. Figures 2.5 and 2.6 display the resulting histograms for the biased and unbiased versions. Comparing these two plots immediately highlights the effects of the importance sampling techniques. While the unbiased simulation used 10 times more primary particles, the biased simulation recorded about 3257 times more particles than the unbiased simulation. It is also worth noting a similar relative proportion in the number of particles. This indicates that the biased particle is not favoring any particular physical process; all it does is increase the number of photons without modifying their normal behavior.

The two other histograms depict the energy spectrum of these particles, weighted by their own particle weight. Figures 2.7 and 2.8 focus on the gamma particles themselves and here again, we see a clear increase in the number of gamma hits recorded in the biased simulation. Regardless, both the energy distribution for the biased and unbiased cases practically produce the same mean. We should also mention a couple of features from these spectra that could be used as a sanity check. First, in both plots, we can clearly distinguish a peak right around 511 keV. This peak corresponds to the energy of the photons generated in the electron-positron annihilation process and shows that the simulations are producing physical results. Second, there are multiple energy peaks below 100 keV which correspond to transition energy from lead. These peaks can be seen much better in figures 2.9 and 2.10.

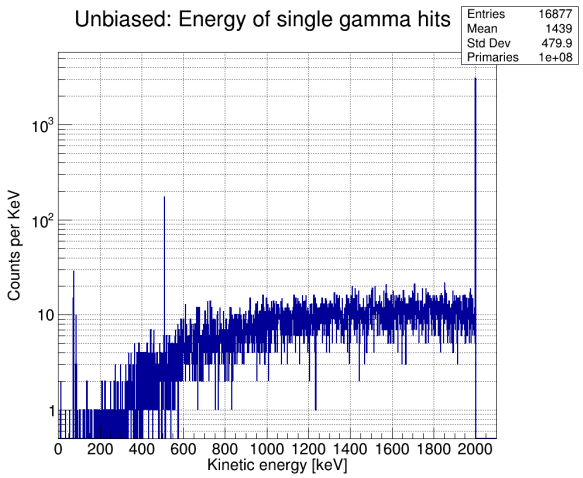

Figure 2.7. Gamma energy spectrum for the unbiased simulation.

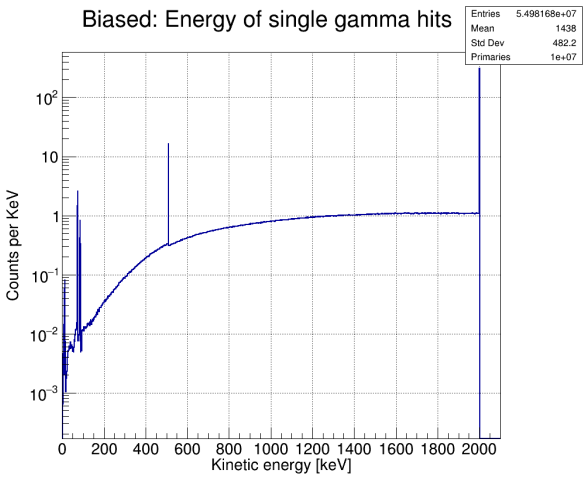

Figure 2.8. Gamma energy spectrum for the biased simulation.

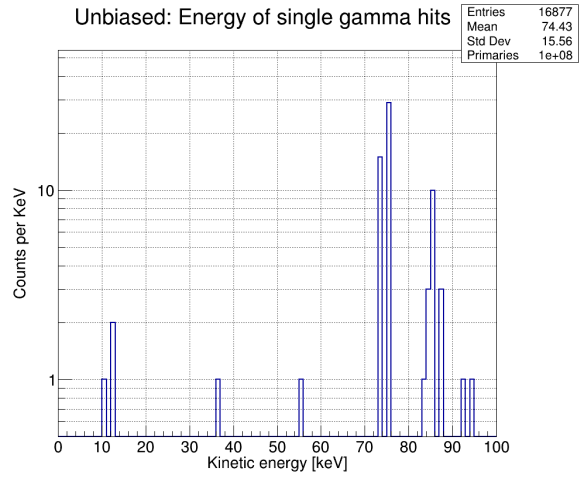

Figure 2.9. Lead lines in the unbiased gamma spectrum.

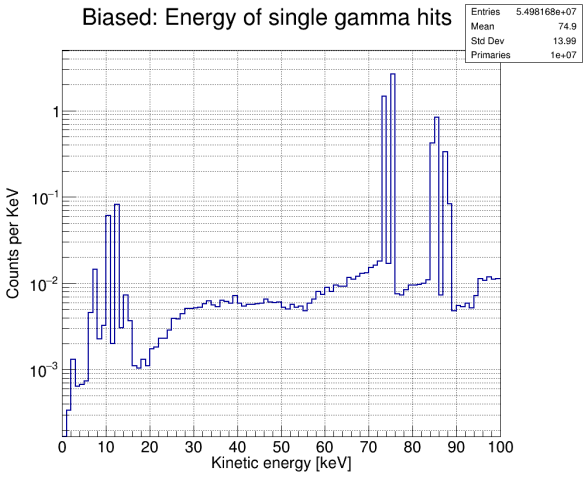

Figure 2.10. Lead lines in the biased gamma spectrum.

This is especially true in the biased case. The peaks between 80 keV and 90 keV correspond to the KN and KM x-ray transitions[**7**], while those between 70 keV and 80 keV correspond to the KL transitions. Similarly, the peaks below 20 keV correspond to the LN and LN x-ray transitions [**7**]. The presence of these spectroscopic peaks is, once again, a good check to verify the physicality of the simulations.

Finally, figures 2.11 and 2.12 gather the energy from the electron and positron hits. The comparison of these two histograms is a great example of the advantages of importance biasing. The unbiased simulation produced an extremely low number of hits, which is certainly not enough to be of any statistical significance. As expected, the biased simulation produced about 3153 times more hits; a factor comparable to the increase seen for the gammas.

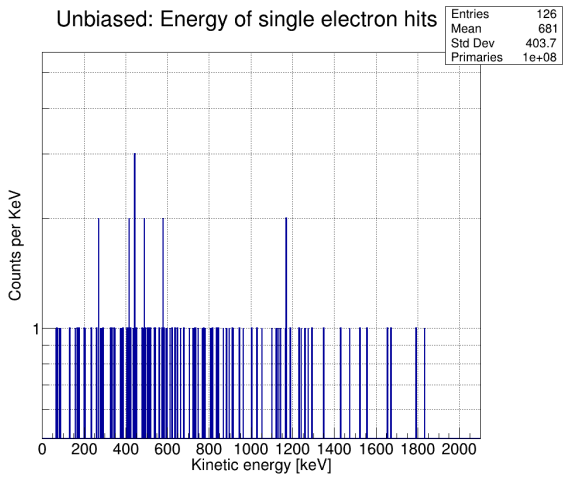

Figure 2.11. Electron energy spectrum for the unbiased simulation.

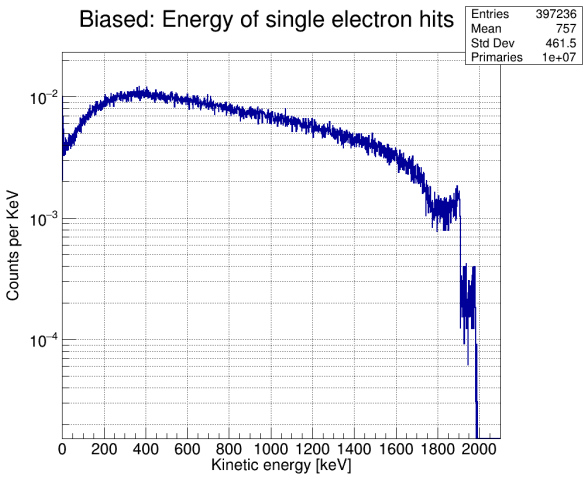

Figure 2.12. Electron energy spectrum for the biased simulation.

In addition to all the physics-related analysis, we must also take a look at the computing side and compare the performance of these two simulations. This is the biggest test for the implementation of this variance reduction technique as the results of this juxtaposition can motivate the further implementation of this technique for other volumes and particle types in SuperSim. Table 2.1 presents a summary of the CPU time and memory used for each simulation run. This data was produced with the cluster's `seff` command but given that this information is only recorded about every 5 minutes, it can be slightly inaccurate. Even so, the results can provide a very good idea of the computational expense of both methods. The last 4 rows of the table give us an overview of the study. The biased simulation was shorter than the unbiased version, with a total runtime of around 39 hours versus 48 hours. Memory-wise, the biased simulation only slightly more memory with a total of 21.6 Gb, compared to 20.9 Gb used by the unbiased case. We must keep in mind that the biased simulation used 10 times fewer primaries than the biased simulation, which is why it is best to compare the computing expense with the quantity "scorer hits per primaries", shown in the before-to-last row of the table. Here, we immediately see the better performance of the biased simulation, since it was capable of producing an average of 32570 times larger than the unbiased simulation, with almost the same amount of computing resources. The last row of table 2.1 reinforces the previous conclusion as well, as the average scorer hits per primaries per CPU time are 5 orders of magnitude larger in the biased case. Similarly, the average scorer hits per primaries per memory are 5 orders of magnitude larger for the biased case, confirming the larger memory use. However, this increased expense is worth it in the long run, as the unbiased simulation would need to run longer or use a larger number of primaries to achieve the same number of hits as the biased simulation, which obviously will use up more memory than the biased version. The analysis of the results also looked for

the number of identical hits. This was done as a way of assessing a possible oversampling of the gammas in the shield. Table 2.1 also compares the number of identical hits, showing that the biased simulation is slightly over-biased. This is indicative of the chosen initial bias length not having an optimal value to preserve correlated detector hits. A longer importance length will reduce this effect, but multiple runs will be necessary to tune this parameter to its optimal value.

	Biased simulation (1×10^6 primaries per run)		Unbiased Simulation (1×10^7 primaries per run)	
Run number	Memory [Gb]	Total CPU time [sec]	Memory [Gb]	Total CPU time [sec]
0	2.16	14301	2.09	16852
1	2.16	14036	2.09	16906
2	2.16	13885	2.09	17438
3	2.16	14067	2.09	17227
4	2.16	14174	2.09	17618
5	2.16	13840	2.09	17413
6	2.16	14278	2.09	16862
7	2.16	14172	2.09	18762
8	2.16	14551	2.09	17823
9	2.16	13954	2.09	17218
Total	21.6	141258	20.9	174119
Total hits recorded at the Inner Poly	55378915		17003	
Total number of identical hits	3655013		0	
(scorer hits-identical hits) / primaries	5.54		1.70×10^{-4}	
Average scorer hits/ particle / resource	2.56×10^{-1}	3.92×10^{-5}	8.14×10^{-6}	9.77×10^{-10}

Table 2.1. Table summarizing the used computing resources

References

[1] R. Agnese, A. J. Anderson, T. Aramaki, I. Arnquist, W. Baker, D. Barker, R. Basu Thakur, D. A. Bauer, A. Borgland, M. A. Bowles, P. L. Brink, R. Bunker, B. Cabrera, D. O. Caldwell, R. Calkins, C. Cartaro, D. G. Cerdeño, H. Chagani, Y. Chen, J. Cooley, B. Cornell, P. Cushman, M. Daal, P. C. F. Di Stefano, T. Doughty, L. Esteban, S. Fallows, E. Figueroa-Feliciano, M. Fritts, G. Gerbier, M. Ghaith, G. L. Godfrey, S. R. Golwala, J. Hall, H. R. Harris, T. Hofer, D. Holmgren, Z. Hong, E. Hoppe, L. Hsu, M. E. Huber, V. Iyer, D. Jardin, A. Jastram, M. H. Kelsey, A. Kennedy, A. Kubik, N. A. Kurinsky, A. Leder, B. Loer, E. Lopez Asamar, P. Lukens, R. Mahapatra, V. Mandic, N. Mast, N. Mirabolfathi, R. A. Moffatt, J. D. Morales Mendoza, J. L. Orrell, S. M. Oser, K. Page, W. A. Page, R. Partridge, M. Pepin, A. Phipps, S. Poudel, M. Pyle, H. Qiu, W. Rau, P. Redl, A. Reisetter, A. Roberts, A. E. Robinson, H. E. Rogers, T. Saab, B. Sadoulet, J. Sander, K. Schneck, R. W. Schnee, B. Serfass, D. Speller, M. Stein, J. Street, H. A. Tanaka, D. Toback, R. Underwood, A. N. Villano, B. von Krosigk, B. Welliver, J. S. Wilson, D. H. Wright, S. Yellin, J. J. Yen, B. A. Young, X. Zhang, and X. Zhao. Projected sensitivity of the supercdms snolab experiment. *Phys. Rev. D*, 95:082002, Apr 2017.

[2] M.J. Berger, J.H. Hubbell, S.M. Seltzer, J. Changa, J.S. Coursey, R. Sukumar, D.S. Zucker, and K. Olsen. Xcom: Photon cross sections database. Technical Report NIST Standard Reference Database 8 (XGAM), Last Update: November 2010, NIST, PML, Radiation Physics Division, 1998.

[3] Carestream. Industrex aa 400 film. `https://www.carestream.com/en/us/medical/products/nondestructive-testing-ndt-solutions/industrex-film-solutions-for-ndt/industrex-film/industrex-aa400-film`.

[4] A. E. Chavarria, J. I. Collar, J. R. Peña, P. Privitera, A. E. Robinson, B. Scholz, C. Sengul, J. Zhou, J. Estrada, F. Izraelevitch, J. Tiffenberg, J. R. T. de Mello Neto, and D. Torres Machado. Measurement of the ionization produced by sub-kev silicon nuclear recoils in a ccd dark matter detector. *Phys. Rev. D*, 94:082007, Oct 2016.

[5] J. I. Collar, A. R. L. Kavner, and C. M. Lewis. Response of csi[na] to nuclear recoils: Impact on coherent elastic neutrino-nucleus scattering. *Phys. Rev. D*, 100:033003, Aug 2019.

[6] John R. de Laeter, John Karl Böhlke, P. De Bièvre, H. Hidaka, H. S. Peiser, K. J. R. Rosman, and P. D. P. Taylor. Atomic weights of the elements. review 2000 (iupac technical report). *Pure and Applied Chemistry*, 75(6):683–800, 2003.

[7] R.D. Deslattes, E.G. Kessler Jr., P. Indelicato[1], L. de Billy[1], E. Lindroth[2], J. Anton[2], J.S. Coursey, D.J. Schwab, J. Chang, R. Sukumar, K. Olsen, and R.A. Dragoset. X-ray transition energies database. Technical Report NIST Standard Reference Database 128, Last update: September 2005, NIST, Physical Measurement Laboratory and [1]Laboratoire Kastler-Brossell, Ecole Normale Supérieure et Univ. P. et M. Curie, France and [2]Stockholm University, Dept. of Atomic Physics, Sweden, 2003.

[8] Brian L. Dougherty. Measurements of ionization produced in silicon crystals by low-energy silicon atoms. *Phys. Rev. A*, 45:2104–2107, Feb 1992.

[9] Geant4. User's guide: For application developers, version 10.6v2. `https://geant4-userdoc.web.cern.ch/UsersGuides/ForApplicationDeveloper/BackupVersions/V10.6c/html/index.html`.

[10] G. Gerbier, E. Lesquoy, J. Rich, M. Spiro, C. Tao, D. Yvon, S. Zylberajch, P. Delbourgo, G. Haouat, C. Humeau, F. Goulding, D. Landis, N. Madden, A. Smith, J. Walton, D. O. Caldwell, B. Magnusson, M. Witherell, B. Sadoulet, and A. Da Silva. Measurement of the ionization of slow silicon nuclei in silicon for the calibration of a silicon dark-matter detector. *Phys. Rev. D*, 42:3211–3214, Nov 1990.

[11] J. H. Gibbons, R. L. Macklin, and H. W. Schmitt. $\mathrm{v}^{51}(p,n)\mathrm{cr}^{51}$ reaction as a 5- to 120-kev neutron source. *Phys. Rev.*, 100:167–168, Oct 1955.

[12] J. H. Hubbell and S. M. Seltzer. Tables of x-ray mass attenuation coefficients and mass energy-absorption coefficients from 1 kev to 20 mev for elements z = 1 to 92 and 48 additional substances of dosimetric interest. Technical Report NIST Standard Reference Database 126, Last update: July 2004, National Institute of Standards and Technology, 1996.

[13] F. Izraelevitch, D. Amidei, A. Aprahamian, R. Arcos-Olalla, G. Cancelo, C. Casarella, A. E. Chavarria, P. Collon, J. Estrada, G. Fernández Moroni, Y. Guardincerri, G. Gutiérrez, A. Gyurjinyan, A. Kavner, B. Kilminster, J. Liao, Q. Liu, M. López, J. Molina, P. Privitera, M. A. Reyes, V. Scarpine, K. Siegl, M. Smith, S. Strauss, W. Tan, J. Tiffenberg, and L. Villanueva. A measurement of the ionization efficiency of nuclear recoils in silicon. *Journal of Instrumentation*, 12(06):P06014, jun 2017.

[14] T. H. Joshi, S. Sangiorgio, A. Bernstein, M. Foxe, C. Hagmann, I. Jovanovic, K. Kazkaz, V. Mozin, E. B. Norman, S. V. Pereverzev, F. Rebassoo, and P. Sorensen. First measurement of the ionization yield of nuclear recoils in liquid argon. *Phys. Rev. Lett.*, 112:171303, May 2014.

[15] Brian Lenardo, Jingke Xu, Sergey Pereverzev, Oluwatomi A. Akindele, Daniel Naim, James Kingston, Adam Bernstein, Kareem Kazkaz, Mani Tripathi, Connor Awe, Long Li, James Runge, Samuel Hedges, Peibo An, and Phil S. Barbeau. Measurement of the ionization yield from nuclear recoils in liquid xenon between 0.3 – 6 kev with single-ionization-electron sensitivity. 2019.

[16] Jens Lindhard, V. Nielsen, Morten Scharff, and P. V. Thomsen. Integral equations governing radiation effects. (notes on atomic collisions, iii). 1963.

[17] C.-P. Liu, Chih-Pan Wu, Hsin-Chang Chi, and Jiunn-Wei Chen. Model-independent determination of the migdal effect via photoabsorption. *Phys. Rev. D*, 102:121303, Dec 2020.

[18] R. K. Romani, P. L. Brink, B. Cabrera, M. Cherry, T. Howarth, N. Kurinsky, R. A. Moffatt, R. Partridge, F. Ponce, M. Pyle, A. Tomada, S. Yellin, J. J. Yen, and B. A. Young. Thermal detection of single e-h pairs in a biased silicon crystal detector. *Applied Physics Letters*, 112(4):043501, 2018.

[19] A R Sattler. Ionization produced by energetic silicon atoms within a silicon lattice. *Physical Review (U.S.) Superseded in part by Phys. Rev. A, Phys. Rev. B: Solid State, Phys. Rev. C, and Phys. Rev. D*, 138, 6 1965.

[20] J Tiffenberg. Results from the antonella experiment,. workshop: calibration of low energy particle detectors (Chicago, IL), September 23rd-25th, 2015.

[21] P. Zecher, D. Wang, J. Rapaport, C. J. Martoff, and B. A. Young. Energy deposition of energetic silicon atoms within a silicon lattice. *Phys. Rev. A*, 41:4058–4061, Apr 1990.

Appendix A

Tower Assembly Work

As part of my efforts for the SuperCDMS, I spent 4 weeks at Stanford University's SLAC National Accelerator Laboratory. During this time, I worked as a collaborator on the preparation of the four detector towers that will finally be used underground at SNOLAB. Throughout the first week, I was formed in the multiple clean room protocols as well as helping with the crating of the first tower. The following two weeks were focused on the testing of tower 2 and the assembly of tower 3. In the last week, the team completed the crating of towers 2 and 3 and the scribbling of multiple parts that will also be used in the SNOLAB experiment.

The element to highlight during my stay at SLAC is the training on the multiple protocols that need to be followed in the clean room and when handling the parts of the detector or the towers. In order to minimize exposure to dust and other ambient contaminants, all of the work related to the detectors and their towers must be performed in a clean room with a very low count of particles per cubic meter. Anyone needing to complete any task or shadow as an observant in the clean room must endure low levels of contamination, by following protocols such as using clean shoes to enter the gowning room, wearing full-body bunny suits, double gloves, shoe covers, hair and beard nets, face masks and bouffant caps. Other protocols to follow include the constant work under a vertical laminar flow hood when assembling the towers, always changing the outermost layer of gloves before handling any tower or detector element, ensuring constant lubrication with ethanol when assembling the towers, and storing the pieces and electronics parts in a purge cabinet under a Nitrogen atmosphere. The last set of guidelines to highlight concerns the handling and transport of the towers once they are assembled. In this case, it is very important to familiarize oneself with the procedures before setting to complete any task; actions such as installing a tower in the test fridge or placing it in a housing to ready the tower for shipping, require the presence of multiple experts, and the SuperCDMS protocols for these processes enforces constant and clear communication among all the parts at crucial stages. All of this training will prove to be quite useful in the

future, as the tower installation at SNOLAB will happen within the next year or so, and I will be able to assist in multiple stages of the installation.